CHARACTERIZATION OF SECONDARY ATOMIZATION AT HIGH OHNESORGE NUMBERS

by

Vishnu Radhakrishna

A Thesis

Submitted to the Faculty of Purdue University

In Partial Fulfillment of the Requirements for the degree of

Master of Science in Aeronautics and Astronautics

School of Aeronautics & Astronautics

West Lafayette, Indiana

December 2018

THE PURDUE UNIVERSITY GRADUATE SCHOOL
STATEMENT OF COMMITTEE APPROVAL

Dr. Paul E. Sojka, Co-Chair

Department of Mechanical Engineering

Dr. Timothée Pourpoint, Co-Chair

Department of Aeronautics and Astronautics

Dr. Guillermo Paniagua Perez

Department of Mechanical Engineering

Approved by:

Dr. Weinong Chen

Head of the Graduate Program

To my family

ACKNOWLEDGMENTS

I would like to extend my deepest sense of gratitude to those who have been instrumental in making this thesis possible.

Words cannot describe my gratefulness to Professor Paul E. Sojka, for first trusting me with this opportunity, and for being a great advisor. The kind of support and understanding he extended made my life much easier at Purdue. Coming into Purdue as a master's student, it was my dream to work with him. Presenting this thesis under his guidance is the surely the proudest moment in my life. He always appreciated individual thinking and challenged me with thought provoking questions. The knowledge I have gained from him, not just as a student but also a human being is priceless. I thank him for making me realize that dreams come true indeed.

I would like to thank my committee members, Dr. Guillermo Paniagua Perez and Dr. Timothée Pourpoint, for their valuable time, and especially Prof. Paniagua for being my well-wisher throughout the course of my masters. He has guided me through my difficult times and always been a pillar of support.

Big thanks to Dr. Jun Chen for his valuable technical inputs during experimentation. Every discussion I have had with him enabled me to come up with smarter ideas.

I would also like to thank my lab mates LongChao Yao, and Weixiao Shang for their time. Their support helped me to stay positive at every hurdle. I would also like to thank Jennifer Ulutas and Tania Bell at Zucrow for helping me with all the official works.

I am very grateful to Dr. Vayalakkara Sivadas, my undergraduate advisor, for introducing me to the field of sprays and atomization, indeed to fluid dynamics itself, and for encouraging me to take up graduate studies.

I am forever indebted to my parents and my sister for all the sacrifices they have made just to enable me to pursue my interest. Without their love and support, I am nothing.

TABLE OF CONTENTS

LIST OF TABLES

LIST OF FIGURES

NOMENCLATURE

Dimensional

A_{probe}	probe area [m^2]
a	drop acceleration [m/s^2]
c	velocity of sound [m/s]
D_{10}	drop or fragment arithmetic mean diameter [m]
D_{30}	drop or fragment volume mean diameter [m]
D_{32}	drop or fragment Sauter mean diameter [m]
D_{43}	drop or fragment de Brouckere mean diameter [m]
d_0	initial drop diameter [m]
$f_0(D)$	fragment number PDF
$f_3(D)$	fragment volume PDF
J_{air}	momentum flux of air [kg/s^2-m]
J_{par}	momentum flux of seed particles [kg/s^2-m]
MMD	mass median diameter [m]
$\dot{n}$	number of seed particles per unit time [1/s]
p	pressure [N/m^2]
$\vec{r}$	radius [m]
t	time [s]
T_{ini}	breakup initiation time
T_{tot}	total breakup time
U_{rel}	relative velocity between drop and ambient fluid along main flow direction [m/s]

U_{core}	velocity of core relative to ambient fluid [m/s]
$\overline{U}_f$	mean relative velocity of fragments in stream-wise direction [m/s]
U_{lag}	relative velocity between air and seed particles [m/s]
V_x	Air velocity in axial direction
δ	boundary layer thickness [m]
λ	wavelength [m]
λ_{vortex}	vortex street length
μ	viscosity of air [kg/m-s]
μ_d	viscosity of drop
ρ	density [kg/m^3]
σ	interfacial tension [kg/s^2]
ω	vorticity

Non-Dimensional

La	Laplace number; $La = Oh^{-2}$
Ma	Mach number; $\frac{U_0}{c}$
N	viscosity ratio; $\frac{\mu_d}{\mu}$
Oh	Ohnesorge number; $\frac{\mu_d}{\sqrt{\rho_d d_0 \sigma}}$
Re	gas-phase Reynolds number; $\frac{\rho_a U_0 d_0}{\mu}$
τ	dimensionless time; $tU_0\varepsilon^{-0.5}d_0^{-1}$
We	Weber number; $\frac{\rho_a U_0^2 d_0}{\sigma}$
We_c	critical Weber number

$We_{cOh\to 0}$	critical Weber number at low Ohnesorge number
$We_{D_{32}}$	Weber number based on Sauter mean diameter
ε	density ratio; $\frac{\rho_d}{\rho_a}$

Subscripts

$_0$	initial
$_a$	ambient phase (experimental)
$_{cro}$	cross-stream
$_d$	drop phase (experimental)
$_{max}$	maximum
$_n$	normal
$_{str}$	stream-wise
$_t$	tangential

ABSTRACT

Author: Radhakrishna, Vishnu. MSAAE
Institution: Purdue University
Degree Received: December 2018
Title: Characterization of Secondary Atomization at High Ohnesorge Numbers
Committee Chair: Dr. Paul E. Sojka and Dr. Timothée Pourpoint

A droplet subjected to external aerodynamic disturbances disintegrates into smaller droplets and is known as secondary atomization. Droplet breakup has been studied for low Ohnesorge (***Oh*** **<** 0.1) numbers and good agreement has been seen amongst researchers. However, when it comes to cases with high the ***Oh*** number, i.e. atomization where the influence of viscosity is significant, very little data is available in the literature and poor agreement is seen amongst researchers.

This thesis presents a complete analysis of the modes of deformation and breakup exhibited by a droplet subjected to continuous air flow. New modes of breakup have been introduced and an intermediate case with no droplet fragmentation has been discovered. Further, results are presented for droplet size-velocity distributions. In addition, Digital in-line holography (DIH) was utilized to quantify the size-velocity pdfs using a hybrid algorithm. Finally, particle image velocimetry (PIV) was employed to characterize the air flow in the unique cases where drops exhibited no breakup and cases with multiple bag formation.

A droplet subjected to external aerodynamic disturbances disintegrates into smaller droplets and is known as secondary atomization. Secondary breakup finds relevance is almost every industry that utilizes sprays for their application.

CHAPTER 1. INTRODUCTION

Atomization is the transformation of a bulk liquid into a multiplicity of small drops (Lefebvre, 1981). Secondary atomization is of utmost importance in a variety of industries working towards the development of science and technology to make human life simpler. injection of gelled hypergolic fuels, internal combustion engines, coatings, Mass spectrometry, agricultural equipment, and materials processing are a few examples.

To accomplish the application specific design requirements, researchers have been working in the field spray theory for years. To better characterize a spray process, atomization has been classified into primary and secondary breakup. Liquid in the form of either jets and sheets breakup in the presence of external disturbances (aerodynamic shearing, electric charge, acoustic) to produce ligaments and droplets, defined as primary breakup. These ligaments or droplets undergo further breakup to produce smaller droplets defined as secondary atomization.

The fundamental processes involved in all the above industries are similar. However, each of these fields requires atomization properties unique to their application. Few industries require a wide range of drop size-velocity distribution while other may require a narrow distribution. industries may also demand either small or large sized drops based on their application. Hence, it is essential to have a thorough knowledge of the influence of fluid physical properties, atomizer geometry and operating parameters on drop size and velocity distributions. Few examples are mentioned below.

Combustion requires secondary drops to be small enough to enhance evaporation and mixing rates. Initial droplet-size distribution can influence the burning characteristics in fuel sprays. Therefore, liquid-fueled combustion processes can be enhanced by optimizing the size-velocity distribution of fuel sprays. In contrast, agricultural industries demand droplets of moderate sizes as small droplets undergo droplet drift due to ambient air flows. Pharmaceutical industries are critical about the droplet sizes so that the drug delivery to the target is accurate. In respirable sprays of medicinal products, drops smaller than 3 μm are ejected from the body during exhalation while, drops greater than 10 μm in diameter are trapped in the respiratory system and doesn't reach the targeted location. In automotive industries, paint spray efficiencies are dictated by the width of drop size distributions since small drops follow the air flow to deposit over the target surface compared to larger droplets. Attaining control over spray process to limit the drops to desired size distributions will be very useful in these situations.

Depending on the liquid properties and the forces on the droplet, several secondary breakup modes can be observed. The ability to model these breakup modes analytically and numerically allows for optimization of design performance in agricultural sprays, pharmaceutical tablet coating, and engine efficiency and emission.

Secondary atomization of Newtonian fluids is something that has been widely studied in recent decades, and several research groups have modeled these breakup modes. Individual studies for intricate cases of Newtonian secondary atomization have been conducted by a number of researchers, including Ranger & Nicholls (1969), Liu and Reitz (1993), Hsiang and Faeth (1992, 1993, 1995), Theofanous (2004), and Guildenbecher *et al.* (2009), to name a few. It is important to understand the underlying physics behind drop deformation and breakup before characterizing the drop size-velocity distributions.

Different breakup modes occur for both Newtonian and non-Newtonian fluids and are determined by the Weber number, which compares the disruptive aerodynamic forces to the droplet surface tension, and the Ohnesorge number, which measures the effects of the droplet viscosity. For low Ohnesorge fluids ($Oh < 0.1$), the following five breakup modes have been identified (See figure 1.1): vibrational ($We < 11$), bag ($11 < We < 35$), multi-mode ($35 < We < 80$), sheet thinning ($80 < We < 350$), and catastrophic ($We > 350$). Where Weber number (We) is defined as

$$We = \frac{\rho_a V_{rel}^2 d_0}{\sigma}. \tag{1.1}$$

and Ohnesorge number is given by

$$Oh = \frac{\mu_d}{\sqrt{\sigma \rho_d d_0}} \tag{1.2}$$

Where ρ_a is the density of the air surrounding the drop, V_{rel} is the relative velocity between the droplet and freestream. $d_0$is the initial drop diameter, σ is the surface tension, ρ_d and μ_d are the droplet density and viscosity respectively.

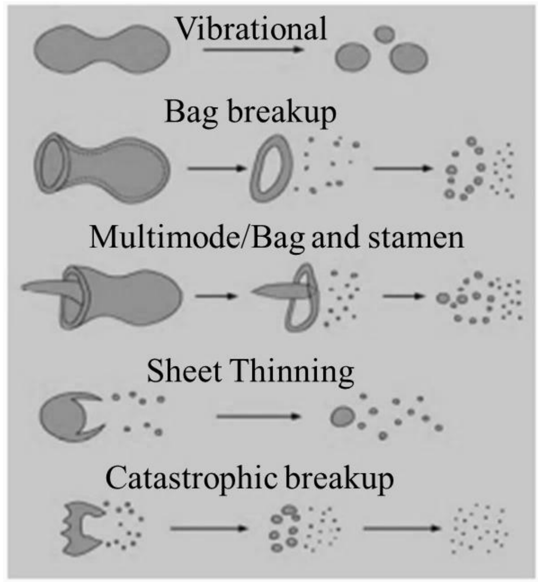

Figure 1.1 Commonly accepted breakup modes for Newtonian drops (Pilch and Erdman, 1987)

The vibrational breakup is rarely observed. It occurs when droplet oscillates at its natural frequency, producing fragments with sizes comparable to parent drop size. Bag breakup consists of a hollow thin membrane like bag attached to a toroidal rim. The toroidal rim consists of the droplet core. The bag disintegrates to produce large number of small-sized droplets, while the rim produces a small number of large ligaments. Multimode/Bag and stamen breakup are similar to bag breakup, but with the addition of arising from the bag in the direction opposite to the droplet motion. The bag first breaks up, followed by the rim breakup and later the stamen dissociates into fragments. Hence, producing secondary drops in a variety of sizes. In sheet thinning regime, secondary drops strip off from the drop periphery. A large number of droplets are produced due to the dominant aerodynamic forces. The droplet core may move downstream without undergoing any breakup. Finally, during catastrophic breakup, the droplet dissociates into a small number of large fragments, which go on to break up further to produces smaller secondary drops.

Brodkey (1967), characterized these breakup modes based on Weber number. The minimum Weber number for a droplet to exhibit a particular mode of breakup was defined as the critical Weber number, given below:

$$We_C = 12(1 + 1.077Oh^{1.6}) \qquad Oh < 10 \tag{1.3}$$

Gelfand (1996) proposed a similar analysis and found the critical Weber number to be:

$$We_C = 12(1 + 1.5Oh^{0.74}) \qquad Oh < 4 \tag{1.4}$$

It is evident from equations 1.3 and 1.4 that Ohnesorge number plays a major role in characterizing the breakup modes. This is of high relevance in industries that deal with high viscous sprays. Very limited work has been done at high Ohnesorge numbers, and, there is a poor agreement amongst researchers for the data that is available. Hsiang and Faeth (1995), constructed a *We* Vs *Oh* map (figure 1.2) to represent the droplet behavior for various Ohnesorge numbers at varying Weber numbers.

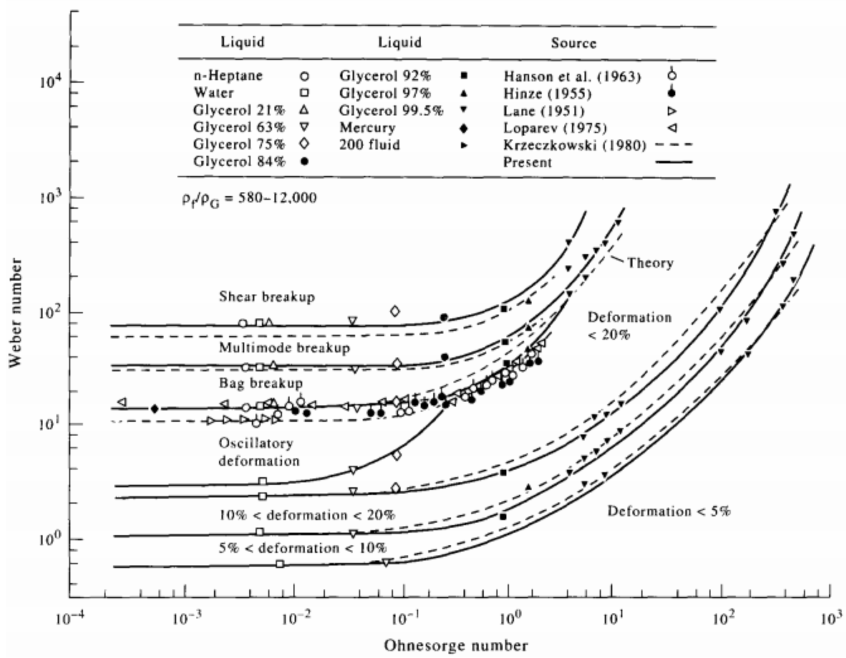

Figure 1.2 *We* versus Oh breakup mode plot for Newtonian drops (Hsiang and Faeth, 1995)

As mentioned earlier, droplet size-velocity distribution plays a crucial role in characterizing secondary atomization. Simmons (1977a, b), studied the drop size distributions and provided a relation between mass median diameter and Sauter mean diameter (D_{32}) (Equation 1.5), and the drop diameter number pdf, f_3(D), approximately as a root-normal given by equation 1.6 (Tate and Marshall,1953).

Finally, Simmons (1977a, b) found the maximum fragment size to be approximately three times MMD.

$$\frac{MMD}{D_{32}} = 1.2 \tag{1.5}$$

$$f3\,(\mathrm{D}) = \frac{1}{2\sigma_{RN}\sqrt{2\pi D}}\,exp\left\{-\frac{1}{2}\left[\frac{\sqrt{D}-\sqrt{\overline{D}}}{\sigma_{RN}}\right]^2\right\} \tag{1.6}$$

Where, σ_{RN} is the distribution width and $\overline{D}$ the mean diameter.

There is sufficient literature discussing the characterization of a representative drop diameter in a spray. However, very little work has been done on the characterization of drop size distribution. Babinsky and Sojka (2002), reviewed the three available methods for modeling drop size distribution: maximum entropy method, discrete probability function method and the empirical method. The empirical method, though easy to use, couldn't predict the distribution. ME method focused on the initial and final stages of the atomization process, and hence it requires more information about resulting drop size distribution than is possible to predict using other means. It was also concluded that DPF method could be used only for primary atomization and hence, secondary atomization required methods like maximum entropy formulation.

A. Déchelette et al. (2011), discussed the concepts of drop size distributions, moments of those distributions, and characteristic drop diameters computed from them. Their conclusions were similar to Babinsky and Sojka (2002). Additionally, they also stated that Stochastic methods can be successfully utilized in numerical models applied to primary and secondary atomization. However, their applications are limited to high-Weber number regimes and hence, cannot predict drop sizes in sprays for which fragmentation cascade cannot be assumed

As mentioned earlier most works were carried out for low viscous fluids. The process of secondary atomization at high Ohnesorge number ($Oh \geq 0.1$), where there is a significant influence of viscosity is still not understood well. It is important to study the properties of atomization at high Ohnesorge number due to its application in fields like spray paints, food processing, and pharmaceutical industries where the fluids used are highly viscous. In addition to these, inelastic non-Newtonian hypergolic fuels are being used in rocket fuel injection, where fluid viscosity is high. Also, in modern diesel and gas turbine engines at low-density ratios, the compression ratio is such that the injected fuel may approach the thermodynamic critical point. Under such circumstances, the *Oh* approaches infinity as the surface tension goes to zero. Currently, no experimental secondary breakup data exists at or near the critical point. DNS studies, such as the work of Han and Tryggvason (2001) and Aalburg et al. (2003), where markedly different breakup characteristics are at predicted very high *We* and *Oh* and very low-density ratios. In addition, current experimentally determined correlations involving high *Oh* are limited and poor agreement is seen between researchers.

The motivation for this work comes from the urge to solve the uncertainties associated with secondary atomization at high Ohnesorge number ($Oh \geq 0.1$). Based on the importance of droplet size-velocity distribution to control the spray processes and the demand to study atomization of high viscous fluids, this thesis focuses on studying the breakup processes associated with secondary atomization at high Ohnesorge number. Droplet deformation and breakup modes are characterized through shadowgraphy. Digital in-line holography was utilized to present a detailed analysis of the droplet size and velocity distributions. Additionally, particle image velocimetry is used to study the aerodynamic characteristics affecting the breakup process. This work would help to better understand droplet breakup at high *Oh*, thereby filling the existing void related to secondary atomization at high Ohnesorge numbers.

This thesis begins with a thorough literature review addressing the secondary atomization of Newtonian fluids at high and low Ohnesorge number, and the experimental methods utilized in the past to characterize them. Subsequently, current experimental methods and test conditions are discussed in detail followed by a comprehensive presentation of results obtained. This work is concluded with the summary of the overall research work and suggestions for the future.

CHAPTER 2. LITERATURE REVIEW

The existing literature in secondary atomization has been reviewed and presented thoroughly. The current work focusses on the secondary breakup of Newtonian droplets at high Ohnesorge numbers ($Oh \geq 0.1$). Hence, this review is limited to only Newtonian fluids. First, the Newtonian breakup of drops at low *Oh* is discussed, followed by the limited data available for viscous drops. Next, experimental methods used to characterize the droplet size-velocity pdfs are presented with emphasis on digital in-line holography.

As mentioned in the previous chapter, Newtonian fluids find importance in a wide variety of industries for spray applications. Numerous works have been presented in the past describing the breakup processes. A Liquid jet or sheet undergoes breakup when the fluid ceases to exist as a cohesive entity. This is defined as primary breakup. Liquid fragments undergo further breakup to produce smaller droplets, defined as secondary atomization. This thesis focuses on secondary atomization and hence, the literature review will be limited to that. Droplet breakup initiates when the liquid drop is subjected to a disruptive force (typically, aerodynamic). The freestream flow accelerates around the droplet creating a pressure difference that deforms the droplet. When the aerodynamic forces are high enough to overcome the surface tension forces of the droplet, breakup occurs. In addition to surface tension, drop viscosity can also play a major role. Highly viscous droplets require relatively higher aerodynamic shearing to exhibit drop breakup. Major modes of breakup have been shown in figure 1.1.

2.1 Dimensionless Groups

Secondary atomization is influenced by both physical properties of the liquid and the external flow. Every multiphase flow problem is a complex phenomenon and requires various parameters to completely explain the physics involved. Atomization is one such intricate problem. Hence, researchers have described their findings in terms of non-dimensional groups. These non-dimensional parameters are widely used by the spray community to better represent their results. Major dimensionless terms are presented in table 2.1.

Table 2.1 Dimensionless groups important in Newtonian drop secondary breakup

Dimensionless Group	**Mathematical Expression**
Weber number (*We*)	$\frac{\rho_a V_{rel}^2 d_0}{\sigma}$
Ohnesorge number (*Oh*)	$\frac{\mu_d}{\sqrt{\sigma \rho_d d_0}}$
Reynolds number (Re)	$\frac{\rho_a V_{rel} d_0}{\mu}$
Density ratio (*ε*)	$\frac{\rho_d}{\rho_a}$
Mach number (*Ma*)	$\frac{V_{rel}}{c}$
Viscosity ratio (*N*)	$\frac{\mu_d}{\mu}$

Weber number gives the ratio of aerodynamic forces to the droplet surface tension. As Weber number increases, aerodynamic forces dominate over liquid surface tension and hence initiates the breakup. Ohnesorge number represents the influence of liquid viscosity. If the *Oh* is high enough, then the viscosity of the fluid dissipates the energy from the aerodynamic forces and reduce the possibility of breakup. In addition to these, other important dimensionless groups are the Reynolds number, density ratio, viscosity ratio and Mach number accounts for the compressibility effects at high velocities. Reynolds number can be represented as

$$\mathrm{Re} = We^{0.5} Oh^{-1} \varepsilon^{-0.5} N \quad (2.1)$$

In addition to these parameters, turbulence within the multiphase region could create disturbances that can disrupt the droplet (Shraiber et al., 1996). Gelfand (1996) cited that, time duration that the droplet subjected to disruptive forces should be enough to initiate the breakup process. Hence, it is necessary to have a complete understanding of temporal influence on the breakup process. To this extent, Ranger and Nicholls (1969), provided a characteristic transport time, which is used to normalize the drop breakup times.

Equation 2.2 gives the equation for non-dimensional time:

$$\tau = t\,\frac{V_{rel}}{\varepsilon^{0.5} d_0} \tag{2.2}$$

Here, τ is the dimensionless time and t is the dimensional time. This choice of characteristic time noted by Ranger and Nicholls (1969) is applicable at low *Oh*. Faeth et al. (1995) utilized a more appropriate characteristic time for high *Oh*, given by Hinze (1948) and is given as:

$$\tau = \frac{\mu_d}{\rho_a V_{rel}^2} \tag{2.3}$$

2.2 Influence of Weber Number

Weber number and Ohnesorge numbers were used as primary parameters to differentiate between modes of breakup. Though the transition to different modes is a continuous process as Weber number increases, researchers have considered this process to be abrupt, in order to quantify the weber number at which the transition occurs. The transition Weber number and is different for each mode of breakup and has a strong dependence on *Oh*. However, from works of Hsiang and Faeth, (1995) it can be stated that transition weber number between modes of breakup remain constant for *Oh* < 0.1 and can be approximated by the values provided in Table 2.2 (Guildenbecher et al., 2009).

Table 2.2 Transition *We* for Newtonian drops with *Oh* < 0.1

Breakup Mechanism	**Transition**
Vibrational	0 < *We* < ~ 11
Bag	~ 11 < *We* < ~ 35
Multimode	~ 35 < *We* < ~ 80
Sheet Thinning	~ 80 < *We* < ~ 350
Catastrophic	*We* > ~ 350

As mentioned earlier, the transition is a continuous process and hence the values of transition *We* are reported contrarily by different authors. For example, Pilch and Erdman (1987) reported transition between multimode and sheet thinning at *We* = 100, while Hsiang and Faeth (1992) chose *We* = 80, and Gelfand (1996) claimed *We* = 40. In Table 2.2, Guildenbecher et al. (2009) presented the values of Hsiang and Faeth (1992) for transitional *We*, with the exception of the transition between sheet-thinning and catastrophic modes, which was taken from the work of Pilch and Erdman (1987), and the transition between vibrational and bag modes, which is an average of numerous authors. This was done considering the works of most researchers and the overlap between their results.

2.3 Influence of Ohnesorge Number

As mentioned earlier, *We* value for various breakup modes are independent of *Oh* for $Oh<0.1$. However, as *Oh* increases, the transitional weber number depends on the viscous effects. As noted by Faeth et al. (1995), in many high-pressure spray applications, the drop phase approaches the thermodynamic critical point where *Oh* increases rapidly as the surface tension approaches zero and ε decreases. Hsiang and Faeth (1992) mentioned that the breakup modes remain same at high Ohnesorge numbers, but the *We* at which these modes are exhibited may vary due to the influence of viscosity, which slows drop distortion and allows more time for aerodynamic drag to reduce the relative velocity. Joseph et al. (1999), performed shock tube experiments at some of the highest recorded values of *We* and *Oh*. Bag breakup was observed at *We* = 160,000 and *Oh* = 26.6. In contrast, for $Oh < 0.1$, bag breakup is expected to end at *We* = 35. No value of *Oh* was reported at which breakup is impossible.

The flow regime map presented by Hsiang and Faeth (1995), (shown in figure 1.2) shows that higher Weber number is needed for various transitions as *Oh* increases. It was also noted that the oscillatory deformation disappears after $Oh > 0.4$. Hinze (1955) and Krzeczkowski (1980) also noted this effect for the breakup transitions but the behavior is similar for the deformation transitions as well, with the oscillatory deformation regime disappearing entirely for $Oh > 0.4$ as noted earlier. Hinze (1955) concluded that no breakup may occur for cases with $Oh > 2$. Contradictory to the works of Hsiang and Feth who suggested that breakup may not occur for cases at $Oh > 4$.

The relation between transitional *We* and *Oh* is often plotted as shown in Figure 1.2 (Hsiang and Faeth, 1995). Many researchers have formulated a relationship for the critical Weber number We_c and *Oh* based on experimental data.

To describe We_c, Brodkey (1967) proposed the following correlation, confirmed by Pilch and Erdman (1987) for *Oh* < 10:

$$We_c = We_{c\ Oh\to 0}(1 + 1.077Oh^{1.6}) \quad Oh < 10 \tag{2.4}$$

Here, $We_{c\ Oh\to 0}$ is the critical Weber number at low *Oh*. Similarly, Gelfand (1996) presented an equation for critical Weber number based on Russian works and proposed:

$$We_c = We_{c\ Oh\to 0}(1 + 1.5Oh^{0.74}) \quad Oh < 4 \tag{2.5}$$

The correlations do not agree with one another for *Oh* > 3.

There existed a lot of inaccuracies in determining the correlations for high Ohnesorge numbers. This was majorly due to the viscosity of the droplet. Researchers could quantify the aerodynamic influence on droplet breakup. However, there were disagreements among researchers in understanding the influence of Viscosity. Cohen (1994) argued that in the absence of fluid viscosity, the increases surface energy is from the kinetic energy imparted from the ambient flow. He derived a formulation by adding an extra term to the energy equation to account for the drop viscosity, thereby increasing the kinetic energy to initiate breakup. The equation presented is given in equation 2.6.

$$We_c = We_{c\ Oh\to 0}(1 + C.Oh) \tag{2.6}$$

where C has a value between 1.0 and 1.8 that is theorized to be dependent on the breakup mechanism. Hsiang and Faeth (1995) performed a similar analysis and studied the variation of transition Weber number with increasing *Oh*. It is seen from figure 1.2 that transitional Weber numbers increase linearly at high Ohnesorge numbers. Further, Aalburg et al. (2003) noted that the effect of surface tension becomes negligible at very high *Oh* and at the critical condition drop viscous forces balance aerodynamic forces. They suggested a new regime map complementary to Figure 1.2 where the ratio $We^{.5}/Oh$ (equivalent to Re based on drop phase viscosity) becomes constant for *Oh* >> 1. Despite these works, no published correlation is known to be accurate at *Oh* > 1. Hence, it has become necessary to understand the drop behavior at high Ohnesorge numbers. The disagreement amongst researchers regarding the occurrence of breakup at high Ohnesorge numbers serves as a motivation to this work. Current work looks closely into the modes of breakup exhibited at high Ohnesorge numbers.

2.4 Fragment Size and Velocity Distributions

Fragment size-velocity distributions are one of the most important properties of secondary atomization. Plenty of data exist in the formulation of size-velocity distribution for primary breakup. However, very little data is available on size velocity distribution for the secondary atomization. No data has been reported for size-velocity distribution for secondary breakup of a droplet at high *Oh*.

In the past, measurements of fragment sizes have been limited in their accuracy. Rapid solidification of fragments and holography was used to measure the particle sizes in atomization. With the development of optical methods, Particle Doppler Anemometry was used to provide more accurate measurements. However, PDA was difficult to be set up in various experimental configurations. Especially in shock tube experiments, due to the small measurement volumes viable in PDA in comparison to the large region through which droplet passes during secondary atomization. As a result, only limited data are available. Guildenbecher et al. (2012) developed Digital holography reconstruction algorithms to estimate the morphology and depth of non-spherical, absorbing particles. Digital in-line holography is an efficient method to quantify the droplet size-velocity distribution for droplet breakup. A detailed review on this is presented in the upcoming sections.

Drop size distributions are often described by two or more characteristic diameters. Here, the nomenclature of Mugele and Evans (1951) will be used. A representative diameter (Dpq) is given by:

$$D_{p-q} = \left[\frac{\int_0^\infty D^p f_0(D)dD}{\int_0^\infty D^q f_0(D)dD}\right]^{\frac{1}{p-q}} \tag{2.7}$$

where p and q are positive integers and $f_0(D)$ is the number pdf. Arithmetic mean diameter is given by D_{10}, the volume mean diameter by D_{30}, and the Sauter mean diameter as D_{32}. Equation 1.5 shows the relation given by Simmons (1977a, b) for drop size distribution for sprays formed using a large number of aircraft and industrial gas turbine nozzles where secondary atomization plays a vital role in determining the final size distribution. Following the work of Simmons (1977a, b), Hsiang and Faeth (1992, 1993) used holography to measure drop size distributions for *Oh* < 0.1.

Formulations provided by Simmons (1977a,b) was successfully utilized to quantify the drop size distributions for secondary atomization. The final block in determining the drop size distributions is either the D_{32} or MMD. Hsiang and Faeth (1992), formulated an analysis by considering the size of the drop phase boundary layer, which is expected to determine the size of fragments in shear breakup. This yielded:

$$We_{D_{32}} = C\varepsilon^{0.25}Oh^{0.5}We^{0.75} \quad We < 1000,\ Oh < 0.1,\ 580 < \varepsilon < 1000 \tag{2.8}$$

where C is a constant of proportionality, and $We_{D_{32}}$ is given by $We_{D_{32}} = \rho_a D_{32} V_{rel}^2/\sigma$.

For the range of parameters considered, Hsiang and Faeth (1992) used C = 6.2 and Equation 2.8 was found to reasonably predict fragment D_{32}. However, they noted that the range of ε was relatively narrow and further testing was needed. Since Equation 2.8 was derived from the assumed physics of shear type breakup, its applicability to bag and multimode mechanisms is limited. For this reason, Wert (1995) proposed a new correlation for D_{32} based on the physics of bag breakup. Because a large portion of the original drop mass is contained in the toroidal rim, D_{32} was assumed to be governed by the growth of capillary instability waves on this rim. This resulted in the following:

$$We_{D_{32}} = C[We(T_{tot} - T_{ini})]^{2/3} \quad 12 < We < 80,\ Oh < 0.1 \tag{2.9}$$

Where initial breakup time (T_{ini}) was defined by Pilch and Erdman (1987) as the interval required for a drop to deform beyond the oblate spheroid shape and T_{tot} as the time when all fragmentation has ceased. The respective correlations are formulated as:

$$T_{ini} = 1.9(We - We_c)^{-0.25}(1 + 2.2Oh^{1.6}) \qquad We < 10^4, Oh < 1.5 \tag{2.10}$$

$$T_{tot} = 6(We - 12)^{-0.25} \qquad 12 \le We \le 18 \tag{2.11}$$

$$T_{tot} = 2.45(We - 12)^{0.25} \qquad 18 \le We \le 45$$

$T_{tot} = 14.1(We - 12)^{-0.25} \qquad 45 \leq We \leq 351$

$T_{tot} = 0.766(We - 12)^{0.25} \qquad 351 \leq We \leq 2670$

$T_{tot} = 5.5 \qquad 2670 \leq We \leq 10^5$

The above-mentioned distributions were determined experimentally. However, many researchers have formulated drop size-velocity distributions theoretically. Maximum entropy formulation (MEF) is one such theoretical formulation. Here, constraints such as all drops being spherical, mass being conserved, and estimates for momentum and energy transferred to the drops from the surrounding gas are placed on the fragment size and velocity distributions.

Babinsky and Sojka (2002) provide a detailed review on three methods of modeling drop size distributions: Empirical, maximum entropy, and discrete probability function (DPF). Their findings are summarized here. Empirical method though extremely flexible, was found to be severely limited in predicting the distribution. It can be used to predict the drop size distribution produced by different atomizer under different operating conditions by establishing an empirical relationship between atomizer geometry, operating conditions, and the distribution parameters. The maximum entropy method was found to be useful in predicting the drop size distributions especially for secondary breakup, where the breakup physics are highly stochastic in nature. The ME method concentrates only on the initial and final stages of the atomization process, and hence it requires more information about resulting drop size distribution than is possible to predict using other means. It requires two representative diameters to accurately predict the distribution. DPF method, on the other hand, is a better approach as the details of the breakup process can be mathematically described. However, DPF method finds relevance only in primary atomization and cases where the distribution of secondary atomization needs to be quantified, ME method seems to be more appropriate.

Cousin et al. developed a method to predict one characteristic fragment diameter using linear stability theory. However, the lack of similar analytical methods to predict the second characteristic diameter makes this model depend on experimental data heavily.

Dumouchel and Boyaval (1999) expanded on the work of Cousin et al. (1996) stating that the selection of representative diameter is by noting that the choice of representative diameter is vital to the accuracy of the size distribution. For example, De Brouckere mean diameter (D_{43}) is the optimum diameter for determining the volume-based distribution as it is very close to the mean of the distribution. Having made these observations, Dumouchel and Boyaval (1999) provide a recommended method to determine the best choice of model constraints based on the distribution being sought.

Li et al. (2005) noted that the MEF is applicable to isolated systems in thermodynamic equilibrium. However, many sprays do not meet these requirements. Therefore, Li et al. (2005) proposed a new model with additional constraints to track the degree of deviation from the equilibrium assumption. The result was a better fit to experimental data. However, this introduced the need for more characteristic diameters, which are not easy to predict a priori. This study helps to understand some of the reasons for inaccuracies in the MEF. However, the practical application of this method is limited.

Dumouchel (2006) included an ad hoc physical minimum and maximum drop diameter in their MEF analysis. These were based on the observation that infinitesimally small drops are impossible due to the presence of surface tension, as are infinitely large drops due to instabilities. Their results show that a minimum of three parameters must now be known a priori. This only exacerbates the problem. In summary, MEF can be used to correlate the fragment size and velocity distributions. However, MEF cannot be considered predictive because constraints are needed a priori, at least some of which must be determined using experimental measurements or come from ad hoc assumptions.

A few other methods have been proposed to predict fragment size distributions. Zhou et al. (2000) studied the fractal characteristics of sprays both theoretically and experimentally. Their model showed some predictive capability. However, some measurements were needed a priori, and more work is required.

2.5 Digital In-line Holography

Digital in-line holography (DIH) is an optical technique in which a collimated laser beam illuminates an object field (Guildenbecher and Sojka, 2015). The resulting diffraction pattern is digitally recorded, and numerical reconstruction of the volumetric field is performed via solution of the diffraction integral equations (Schnars and Jueptner, 2005). DIH has a number of advantages for quantification of multiphase, particle flows including: (1) individual particles can be located in three dimensional (3D) space; (2) the size and shape of each particle can be measured at their in-focus location; (3) 3D particle velocities can be determined from two or more holograms recorded with short interframe times; (4) non-spherical particles can be quantified; and (5) knowledge of the index of refraction is not necessarily required (Guildenbecher and Sojka, 2015). Due to these advantages, DIH has been explored for applications to flows of gaseous particulates (Tian et al., 2010 and Lebrun et al., 2011), liquid drops, and solid particulates, among many others.

Digital in-line holography numerically reconstructs a recorded hologram using the object wave. Size and position of particles in a 3D domain are detected using this method. Guildenbecher et al. (2012) presented work on the quantification of size and position of particles with non-spherical morphologies. The work, in particular focused, on in-line configuration due to the simplicity of the optical setup and minimal distortions of in-plane morphologies. However, this geometry is also characterized by a large depth-of-focus and high uncertainty in the detected depth. His works also presented a hybrid method that significantly improves the accuracy of the measured depth and particle morphologies. Furthermore, the proposed hybrid method automatically determines the optimum threshold for each particle, and, therefore, requires minimal user inputs. New methods proposed by Guildenbecher et al. (2012) uses non-dimensional parameters, that reduce the simulation time.

Gao et al. (2013) utilized the hybrid method by Guildenbecher et al. (2012) to characterize the multiphase fragmentation using digital in-line holography (DIH). DIH was applied to record sequential holograms of the breakup of an ethanol droplet in an aerodynamic flow field. Further, various stages of the breakup process were recorded, including deformation, bag growth, bag breakup, and rim breakup. The hybrid method proposed by Guildenbecher et al. (2012) was applied to extract the three-dimensional (3D) location and size of secondary droplets as well as the 3D morphology of the rim. Particle matching between sequential frames was used to determine the velocity. A good agreement was found between the results obtained from DIH to that from PDA under similar testing conditions.

The ease of experimental setup and the credibility of the size-velocity distribution obtained from DIH serves as an encouragement to use a similar hybrid DIH method to quantify the size-velocity distribution for secondary atomization at high Ohnesorge numbers which contributed to a major portion of this thesis.

2.6 Particle Image Velocimetry

Inamura et al. (2009) studied the airflow around a single deformed droplet and the velocity distributions were measured by particle image velocimetry. The results showed that vortices are generated on the leeward side of the droplet. For the bag-type breakup, the vortices were generated alternately, similar to a Karman vortex. For the bag-type breakup, the upward air velocity toward the leeward surface of a droplet was found to be less than the downward air velocity toward the windward surface. It was reported that the relative velocity between the upward and downward air velocities bulges the droplet out like a bag. On the other hand, for the umbrella-type breakup, bilaterally symmetrical twin vortices were generated. The upward velocity is almost the same as the downward velocity. Therefore, the center of the droplet remains as a wick and the peripheral part of the droplet bulges out.

Flock et al. (2012) presented the deformation and fragmentation of single ethyl alcohol drops injected into a continuous air-jet is experimentally investigated through PIV. They considered two conditions—one which leads to the bag breakup morphology and one leading to the sheet-thinning morphology. It was found that no significant differences are observed in the structure of the gas-phase wake, indicating that gas-phase flow morphologies may not significantly affect the transition between liquid-phase breakup morphologies.

Jiang and Agarwal (2014) worked on glycerol Atomization in the Near-Field of a Flow-Blurring Injector using Time-Resolved PIV and High-Speed Visualization. Their findings are summarized as follows: formation of thick ligaments and relatively larger droplets at the injector exit resulting from the primary breakup by the FB atomization inside the injector. Thinning of ligaments as they intermingle and interact with the high-velocity atomizing air was noted. Further, it was noted that droplets and ligaments breakup into small droplets with a diameter of around 21 μm.

Very limited data are available on PIV for secondary drop breakup. Hence, it has always been difficult to understand the flow dynamics around the droplet due to the lack of data to support the minimal literature available. There is no work done on PIV to study the breakup of viscous droplets. This thesis serves as a rich material to bridge the void existing in the studies related to aerodynamic influence on secondary atomization. PIV was carried out specially to understand the flow structure in the special modes of deformation exhibited by droplets at high *Oh*.

CHAPTER 3. EXPERIMENTAL APPARATUS AND UNCERTAINTY

Secondary atomization of high viscosity droplets was characterized using various diagnostic techniques. The droplet falls into a continuous air jet for a range of Weber numbers. As the Weber number increases, droplet exhibits various modes of deformation and breakup. Droplet morphology and breakup was characterized using shadowgraphy through high-speed imaging. Size-Velocity *pdfs* were generated through Digital in-line Holography. Particle Image Velocimetry was carried out to understand the aerodynamic influence on droplet breakup. A schematic of the air flow and droplet generation system is shown in figure 3.1.

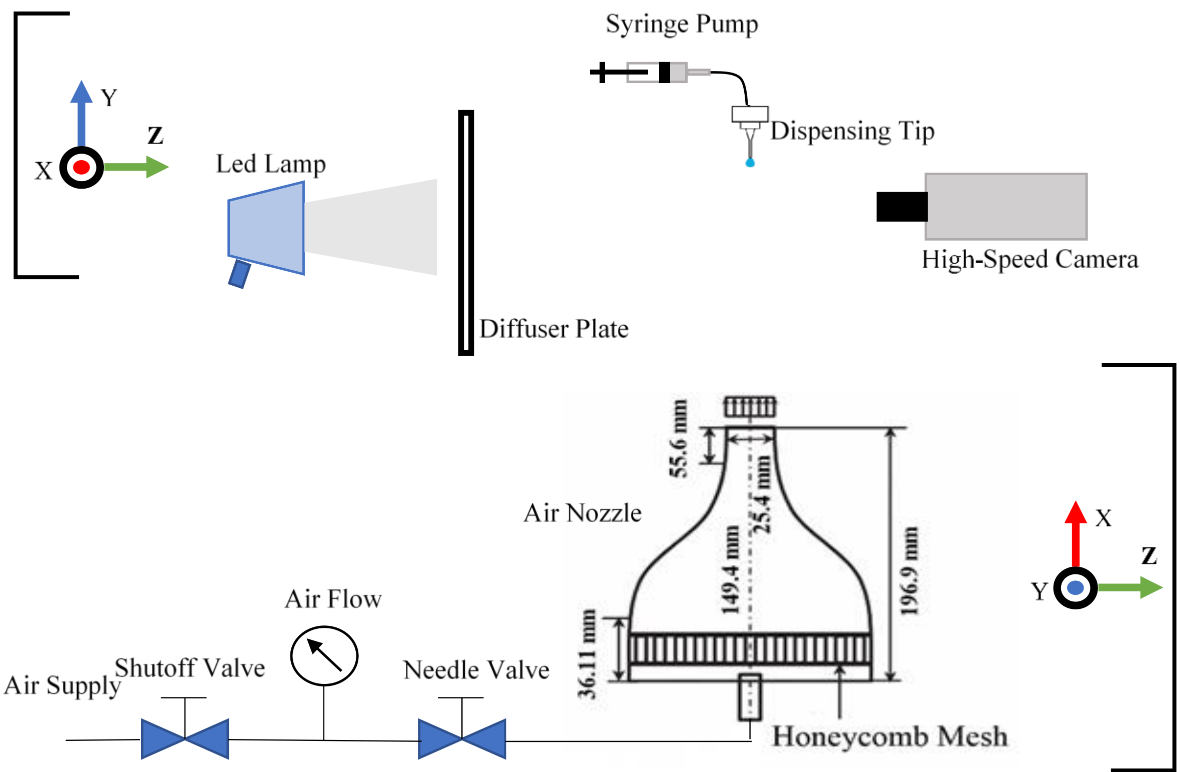

Figure 3.1 Experimental configuration for measuring drop breakup in a high-speed air jet. Top segment is a view along the streamwise (horizontal) axis while the bottom segment is an overhead view

In this chapter, the gas and liquid supplies and the components utilized for the diagnostic techniques are discussed separately. Apparatus utilized for Shadowgraphy (Fig 3.1), DIH and PIV are discussed in detail through a schematic representation. The relative uncertainties associated with flow measurements are also reported (in %).

3.1 Experimental Apparatus

3.1.1 Airflow System

Compressed air with a maximum potential up to 600 kPa was driven from a storage tank to the converging air nozzle. The flow passed through the shutoff valve and a Micro Motion F-Series Coriolis flow meter before being regulated by a needle valve for desired flow rates.

The air nozzle was made from clear acrylic and was designed to produce a nearly uniform velocity profile at its exit, (Guildenbecher, 2009). Figure 3.2 shows the converging nozzle with a 15 cm od entrance chamber and a 2.54 cm exit diameter. Air flows through a 13 mm od tube into the chamber through radial ports to provide uniform flow. The nozzle chamber consists of a 2.54 cm long polycarbonate honeycomb with a cell size of 4 mm. This helps to suppress the large-scale eddies and swirling flow in the nozzle. After this, the air flows through a wire mesh with 0.05 mm diameter and a 0.07 mm space between the wires. This configuration helps to attain a steady, laminar, 1D flow at the exit.

Figure 3.3 shows a *Velmex* 3D translator was utilized to aid the data collection process. It was positioned and controlled using a *UniSlide* stepper motor and an NF90 controller. The *UniSlide* assemblies had 2024-T3 type hardened aluminum sliders with bonded bearing pads of a PTFE composite formulation. They converted rotary-to-linear motion through a precision roll-formed lead screw having a spatial resolution of 5 μm per step. Commands and data to specify the direction of movement and speed were entered through an interface (NF90) attached to a host computer, (Lopez, 2010).

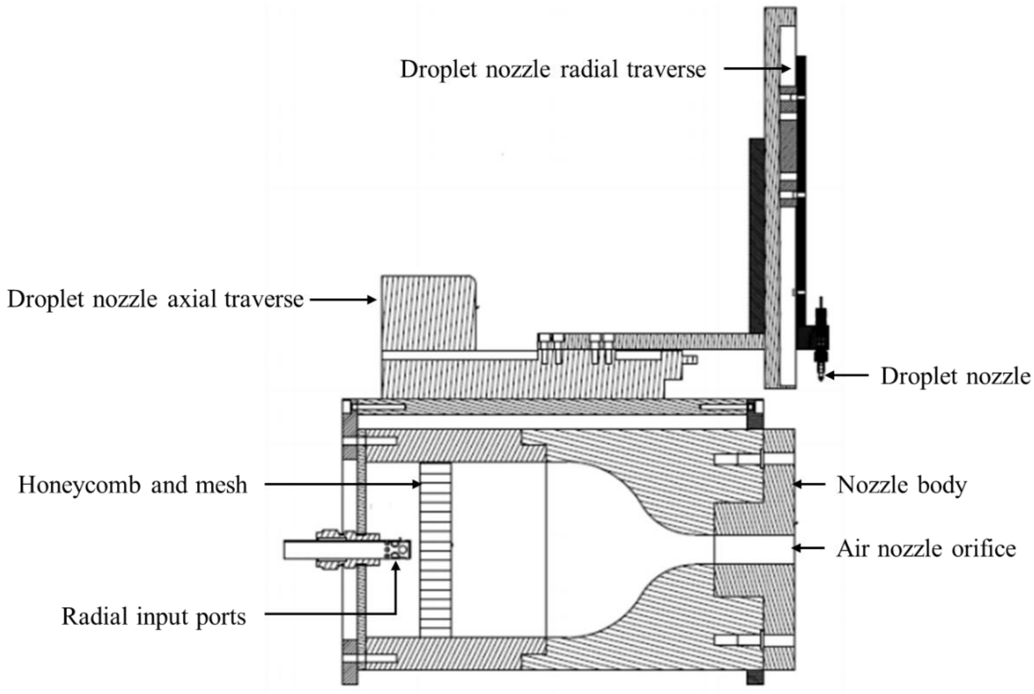

Figure 3.2 Nozzle-Liquid System (Guildenbecher, 2009)

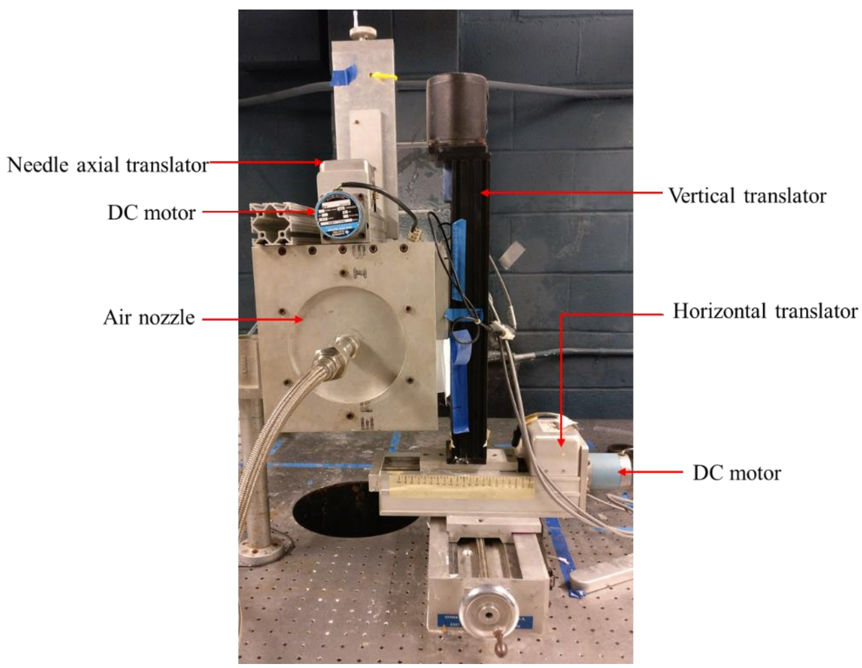

Figure 3.3 Air nozzle and translator setup

3.1.2 Drop Generation

Drop generation system utilized for the experiment was similar to the one used by (Guildenbecher, 2009). Liquid drops of diameter 3 mm were produced using a droplet generator consisting of a syringe pump (NE-300 Just Infusion™) and syringe tip (EFD Dispensing Components Kit 5100).

The liquid drops left the syringe tip with approximately zero velocities and accelerated due to gravity into the high-speed air jet. The drop production rate was sufficiently slow (no greater than 2 Hz), such that the aerodynamic effects of the droplets in the air jet did not interfere with the subsequent drop breakup. Varying the air jet velocity controlled the Weber number.

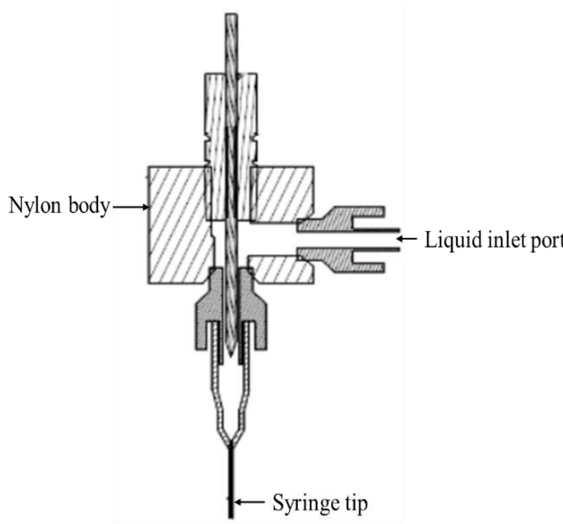

Figure 3.4 Drop Generator (Guildenbecher, 2009)

3.1.3 Image Acquisition

For the shadowgraphy, drops were backlit using a led lamp. The beam falls onto a ground glass diffuser plate to produce 2D shadows of the droplet breakup processes. A Photron SA-Z monochrome camera (20 μm pixel pitch, 12-bit ADC depth) was operated with an exposure time of 6.25 μs capturing images at a rate of 60,000 frames per second and a resolution of 896×368 pixels. The exposure time maximized temporal resolution while providing acceptable contrast. The framing rate is the maximum available at the stated array size. A Nikon AF-Micro Nikkor with a 105 mm focal length and an aperture of f/2.8 was attached to the camera to acquire images located in the focal plane. The images obtained were sampled using *Photron Fastcam Viewer* Ver.3681 (x64) software.

A similar camera-lens combination was put to use for Digital in-line Holography. Images were obtained at a frame rate of 20,000 fps and an exposure time of 6.25 μs. Images had a resolution of 1024 x 1024. The camera used for PIV measurements is an Imperx B4020 advanced high-speed progressive scan, fully programmable CCD camera. It is built around the TRUESENSE KAI-11002 Interline Transfer CCD image sensor which provides an image resolution of 4008 x 2672 and delivers up to 6.4 frames per second with a 43.3mm optical format. The optical setup for DIH and PIV is explained in the upcoming sections.

3.1.4 Digital in-line Holography

The experimental configuration for DIH is described by Guildenbecher and Sojka (2015) and illustrated in Figure 3.5. The illumination source was a Laser Lab Components, Inc. Single Longitudinal Mode Laser, producing up to 300 mW at 532 nm. The output beam was spatially filtered using a ThorLabs Mounted Absorptive Neutral Density Filter (Ø25 mm, SM1-Threaded Mount, Optical Density: 1.0), expanded from ~3 to ~85 mm using a ThorLabs Fixed Optical Mount (FMP1 - Fixed Ø1" Optical Mount, 8-32 Tap), and collimated using a Malvern biconvex lens (600 mm focal length, 2⅜” clear aperture). After the beam passed through the particle field, the resulting diffraction images were recorded at 20 kHz using the high-speed camera.

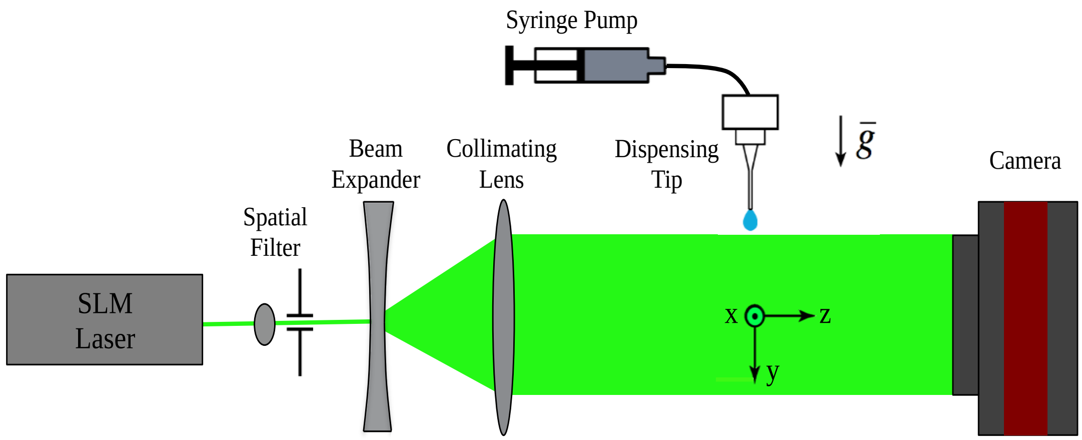

Figure 3.5 DIH experimental configuration

3.1.5 Particle Image Velocimetry

The PIV setup is based on the works of A.K. Flock *et al.* (2012). PIV-system is added to the general experimental configuration as shown in Figure 3.6. A double pulsed Nd:YAG laser (model New Wave Solo III) emits light at 532 nm which passes through a cylindrical lens (Dantec Dynamics) to form a laser sheet with a thickness of about 1 mm. The laser sheet is directed into the test section using a mirror. The air flow setup is a little different compared to the above cases. Flow from the needle valve is bypassed into an oil drop generator (model 9307-6 from TSI Inc.), and then T-ed back to the nozzle. By controlling the ratio of ‘‘air with’’ to ‘‘air without’’ tracer particles entering the nozzle, the density of the seeding can be adjusted. This is done to generate tracer particles with a mean diameter of approximately 1 μm.

To understand the mean droplet behavior, it is necessary to obtain a large dataset. To do so the data acquisition systems are triggered by the falling droplet. This enables us to have a better control over capturing images exhibiting drop deformation. For this, the beam from a helium–neon laser (Uniphase Inc., model 1135P) is projected through the droplet trajectory onto a photodetector (Thorlabs Inc., model DET210). The intensity change, caused by the passing droplet, sends a trigger signal to the timing unit of the PIV/HSS system. Post-processing of raw images was carried out using *LaVision DaVis* Ver.8 software.

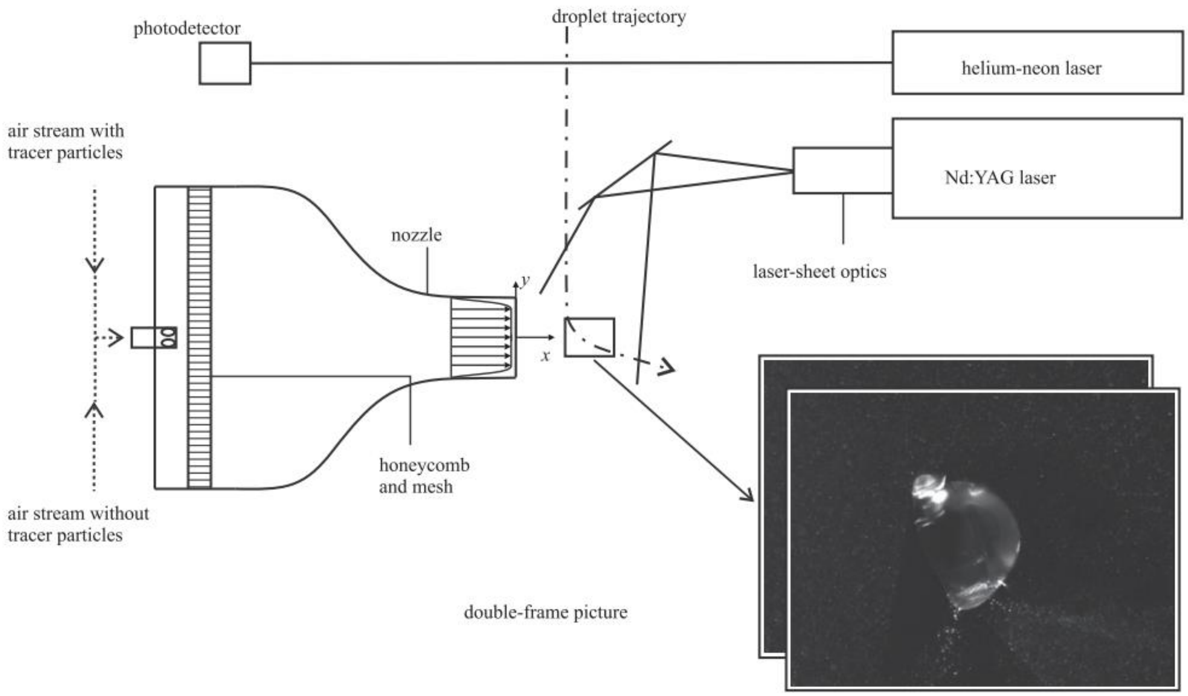

Figure 3.6 Experimental configuration of particle image velocimetry, (A.K. Flock *et al.*,2010)

3.2 Fluid Properties and Uncertainty Analysis

3.2.1 Liquid Characteristics

Two sets of glycerin-water solutions were tested in the current experiment for a range of Weber numbers. Surface Tension was computed using a CENCO Scientific DuNOÜY tensiometer. Viscosity was measured using a falling ball viscometer from HAAKE (B 85081) and densities were characterized by weighing a known volume of the fluid on a Sartorius analytical balance from Pioneer Balances. All solutions were mixed placing it on a magnetic stirrer (Corning PC-620D) for 6-8 hrs. Values for each solution are listed in Table 3.1.

Table 3.1 Physical properties of glycerin-water solution used to generate droplet

Glycerin (ml)	**Water (ml)**	**% Glycerin**	**Density, ρ_d (kg/m^3)**	**Viscosity, μ_l (Ns/m^2)**	**Surface tension, σ (N/m)**
100	11	90.1	1200 ± 30	0.27 ± 0.01	0.0651 ± 0.0002
100	6.3	94.1	1230 ± 30	0.46 ± 0.01	0.0645 ± 0.0002

3.2.2 Airflow Characterization

Air velocity field for the current setup was characterized by Lopez, (2010). Transitional *We* plays a major role in characterizing breakup regimes. This demanded the need to characterize the air flow field. Guildenbecher (2009) and Lopez (2010) made the axial velocity measurements through the nozzle centerline using LDA and PIV. Figure 3.7 shows the results obtained. Axial velocity agreement was noted to be within ± 6%. Additionally, there existed a uniform axial velocity profile across the jet centerline agreeing within ± 4%.

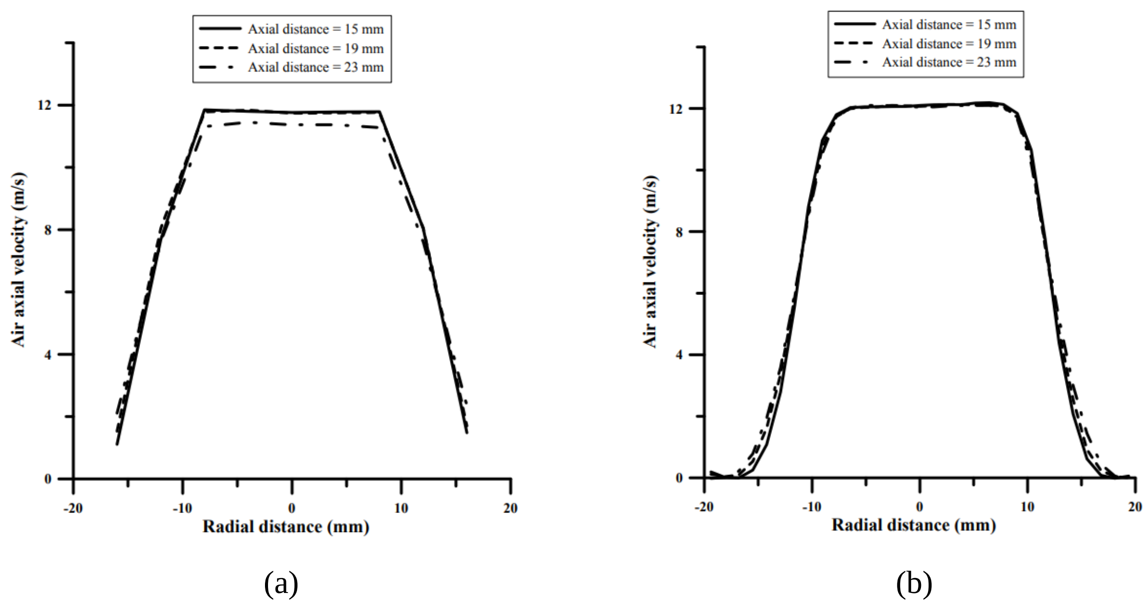

Figure 3.7 Air mean axial velocity (a) obtained using LDA (b) Obtained using PIV (Lopez, 2010)

3.2.3 Uncertainty in Air Flow Rate

The uncertainty in the air flow rate is due to the Coriolis gas flow meter. The least measuring scale on this flow meter is ± 0.0001 kg/min and reads the flow rate to within ± 0.001 kg/min. Therefore, the relative uncertainty was found to be ± 0.16% for the range of data collected.

3.2.4 Uncertainty in Drop Size

Uncertainty in the drop size measurements was calculated from the images recorded using high-speed imaging. The uncertainty in this quantity (u_{d_0}) comes from vagueness at droplet boundary. It was determined to be ± 2.80%.

3.2.5 Uncertainty in Relative Velocity

A significant basis of uncertainty is that concomitant with the determination of relative velocity (V_{rel}). From figure 3.7 it is evident that the LDA and PIV techniques determine the centerline velocity within ± 6. To ensure the seed particles would follow the flow, the velocity lag was determined using stokes flow solution given by:

$$U_{lag} = \frac{\rho_s d_s^2}{18\mu} a \tag{3.1}$$

Here, U_{lag} is the lag velocity, d_s is the seed particle diameter (2 µm), ρ_s is the seed particle density (915 Kg/m^3), µ is the viscosity of air, and a is the acceleration of particles. For equation 3.1 to be valid, the assumption that Re<1 must be satisfied so that inertial and body forces can be neglected. Hence, the model is valid only if the lag velocity is less than 7 m/s.

For an air flow rate of 0.7 kg/min, PIV measurements reveal an average convective acceleration along jet centerline to be 150 m/s^2. Therefore, from equation 3.1, $U_{lag} = 0.002$ m/s. It will eventually be shown that this value is way less than the uncertainty due to turbulent fluctuations. Hence this value can be neglected. Similar calculations at all other flow rates considered resulted in the same conclusion.

In addition to minimizing the effects due to velocity lag, it is important to ensure that momentum transfer from the seeding particles is sufficiently small. From LDV results, it is evident that the concentration of seeding particles is maximum at the jet centerline. Therefore, we choose that location to calculate the momentum transfer from the seeding particles.

Momentum flux of air and seeding particles are calculated from equation 3.2 and 3.3 respectively.

$$J_{air} = \rho_a U_s^2 \tag{3.2}$$

$$J_{par} = \frac{\pi}{6} d_s^3 \rho_s U_s \dot{n} \frac{1}{A_{probe}} \tag{3.3}$$

Where d_s is the mean particle diameter (2 µm), $\dot{n}$ is the number of particles per unit time, and A_{probe} is the probe cross-sectional area. For a similar case where the air flow rate is 0.70 kg/min, $\dot{n}$ was 6700 particles/s and probe are was 1.2 mm^2 with a mean speed of 21 m/s. This gives us a ratio of $\frac{J_{air}}{J_{par}} = 1 \times 10^6$. Hence, indicating that momentum loss from air to seed particles does not contribute to uncertainty in the measurement of air velocity. Hence, using the above explanations it can be justified that the velocity profile of seeding particles meet the criteria to accurately represent the velocity profile of unseeded air.

Lopez (2010) provides a plot of turbulence intensity, which is the main contributor to the uncertainty of the air velocity (see figure 3.8). From this plot, the uncertainty in air velocity is found to be ± 3%. Here, only until radial distance approximately10 mm is considered, as beyond that the boundary layer and mixing layer is encountered (shown in figure 3.7). The drops have zero horizontal velocity as they are vertically falling in this investigation. Hence, V_{rel} is equal to the air velocity U_0 and its uncertainty is given by u_{U_0}.

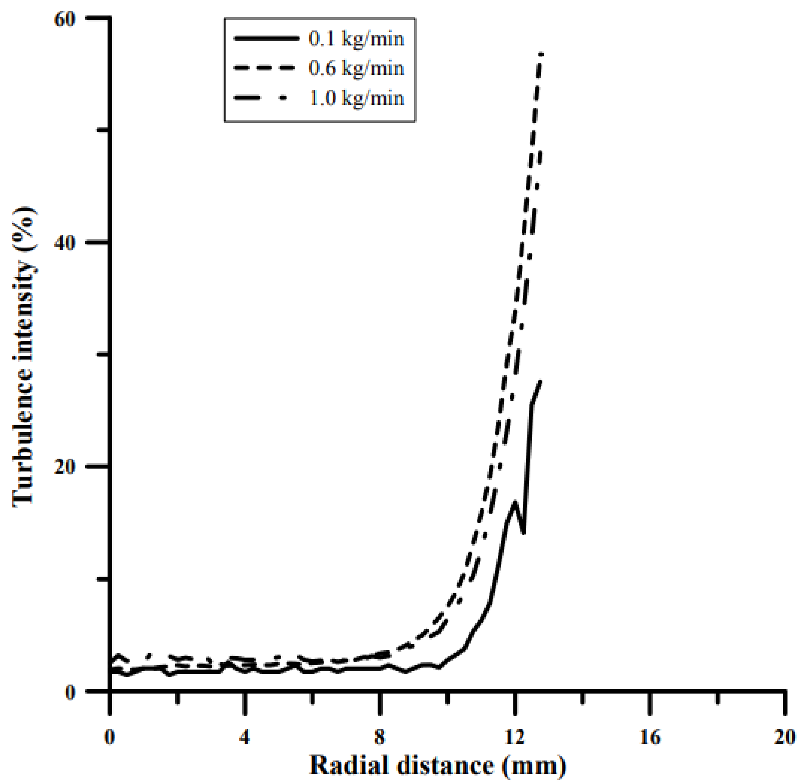

Figure 3.8 Axial turbulence intensity obtained using LDA (Lopez, 2010)

3.2.6 Uncertainty in Weber Number

The uncertainties associated with the non-dimensional parameters are of utmost importance. Guildenbecher (2009), presented the detailed equations to quantify these uncertainties based on the work of Kline and McClintock (1953).

The uncertainty associated with Weber number (u_{We}) is calculated based on the following equations.

$$u_{We} = \left[\left(\frac{\rho_a}{We}\frac{\partial We}{\partial \rho_a} u_{\rho_a} \right)^2 + \left(\frac{U_0}{We}\frac{\partial We}{\partial U_0} u_{U_0} \right)^2 + \left(\frac{d_0}{We}\frac{\partial We}{\partial d_0} u_{d_0} \right)^2 + \left(\frac{\sigma}{We}\frac{\partial We}{\partial \sigma} u_{\sigma} \right)^2 \right]^{\frac{1}{2}} \tag{3.4}$$

Where,

$$\frac{\partial We}{\partial U_0} = \frac{2\rho_0 U_0 d_0}{\sigma} \tag{3.5}$$

$$\frac{\partial We}{\partial d_0} = \frac{\rho_a U_0^2}{\sigma} \tag{3.6}$$

$$\frac{\partial We}{\partial \sigma} = \frac{-\rho_a U_0^2 d_0}{\sigma^2} \tag{3.7}$$

$$\frac{\partial W_e}{\partial \rho_a} = \frac{U_0^2 d_0}{\sigma} \tag{3.8}$$

After appropriate calculations u_{We} was found to be ± 6.10%.

3.2.7 Uncertainty in Ohnesorge Number

Due to the high viscosity of the fluids used, *Oh* tends to be one of the major non-dimensional characteristics associated with the current problem. The uncertainty associated with *Oh* is calculated using the equation 3.6 and is denoted as u_{Oh}.

$$u_{Oh} = \left[\left(\frac{\mu_d}{Oh}\frac{\partial Oh}{\partial \mu_d} u_{\mu_d} \right)^2 + \left(\frac{\rho_d}{Oh}\frac{\partial Oh}{\partial \rho_d} u_{\rho_d} \right)^2 + \left(\frac{\sigma_d}{Oh}\frac{\partial Oh}{\partial \sigma_d} u_{\sigma} \right)^2 + \left(\frac{d_0}{Oh}\frac{\partial Oh}{\partial d_0} u_{d_0} \right)^2 \right]^{\frac{1}{2}} \tag{3.9}$$

Where,

$$\frac{\partial Oh}{\partial \mu_d} = \frac{1}{\sqrt{\rho_d \sigma d_0}} \tag{3.10}$$

$$\frac{\partial Oh}{\partial \rho_d} = -\frac{\mu_d}{2\sqrt{\sigma d_0 \rho_d^3}} \tag{3.11}$$

$$\frac{\partial Oh}{\partial \sigma} = -\frac{\mu_d}{2\sqrt{d_0 \rho_d \sigma^3}} \tag{3.12}$$

$$\frac{\partial Oh}{\partial d_0} = -\frac{\mu_d}{2\sqrt{d_0^3 \rho_d \sigma}} \tag{3.13}$$

Therefore, from the above equations, maximum uncertainty was determined as ± 4.38%

3.2.8 Uncertainty in Reynolds Number

Based on a similar method adopted in previous sections, uncertainty in Reynolds number calculations were also obtained. Reynolds number plays a major role in explaining the PIV results, where the aerodynamic influence on the droplet behavior is explained. The equations employed to obtain u_{Re} are given below.

$$u_{Re} = \left[\left(\frac{\rho_a}{Re}\frac{\partial Re}{\partial \rho_a} u_{\rho_a} \right)^2 + \left(\frac{U_0}{Re}\frac{\partial Re}{\partial U_0} u_{U_0} \right)^2 + \left(\frac{d_0}{Re}\frac{\partial Re}{\partial d_0} u_{d_0} \right)^2 + \left(\frac{\mu}{Re}\frac{\partial Re}{\partial \mu} u_{\mu} \right)^2 \right]^{\frac{1}{2}} \tag{3.14}$$

Where,

$$\frac{\partial \mathrm{Re}}{\partial \rho_a} = \frac{U_0 d_0}{\mu} \tag{3.15}$$

$$\frac{\partial \mathrm{Re}}{\partial U_0} = \frac{\rho_a d_0}{\mu} \tag{3.16}$$

$$\frac{\partial \mathrm{Re}}{\partial d_0} = \frac{\rho_a U_0}{\mu} \tag{3.17}$$

$$\frac{\partial \mathrm{Re}}{\partial \mu} = -\frac{\rho_a U_0 d_0}{\mu^2} \tag{3.18}$$

Hence, the uncertainty in Reynolds number is found to be ± 7.9%.

CHAPTER 4. RESULTS

4.1 Shadowgraphy

Droplet deformation and breakup were considered for a range of Weber numbers, exhibiting different modes of breakup. Shadowgraphy was done for the cases mentioned below to better understand the droplet deformation physics at high *Oh*. Data were collected from the start of deformation for $35 \leq We \leq 120$, in increments of five for $Oh = 1$.

From figure 4.1 for $30 \leq We \leq 40$ the droplet exhibits bag breakup from an initial configuration Hsiang and Faeth [1994] call a "dome." The droplet deformation is like that observed at lower *Oh*, with the bag breakup followed by rim breakup in the range $33 \leq We \leq 38$. As the droplet enters the air jet, it transforms into an oblate shaped structure. This oblate shaped drop develops a bag from its center in the downstream direction. The thin membrane shaped bag first disintegrates to form small droplets while the thick rim, consisting of the droplet core contributes to relatively larger droplets.

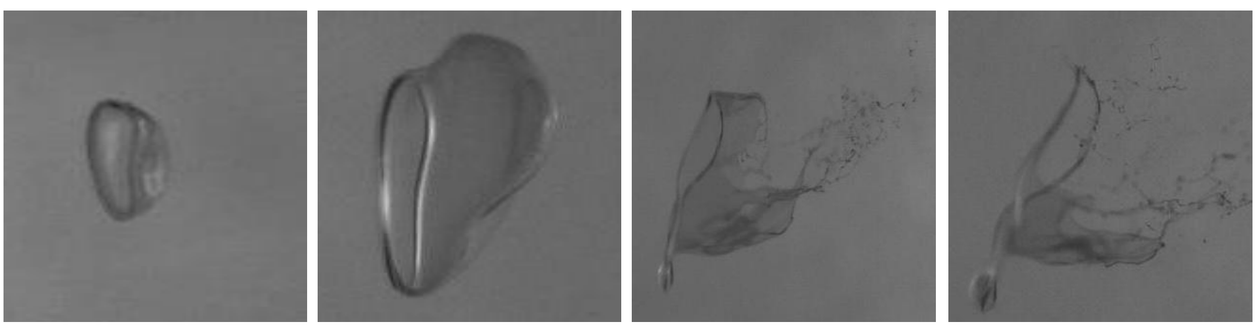

Figure 4.1 Shadowgraphs of drops undergoing aerodynamic fragmentation for $30 \leq We \leq 40$

However, as *We* increase, there is a stamen-like feature arising out of the bag; this mode is either called the bag and stamen or multimode (Figure 4.2). As the bag grows, a stamen projects parallel to the flow and along the windward direction, it disconnects from the rim and remains connected to the bag, then separates from the bag as they break up. After the bag bursts, the rim begins to break up into drops, followed by the stamen. Starting at $We = 40$ the multimode regime begins and continues until $We = 50$. This is consistent with the work of Hsiang and Faeth (1994).

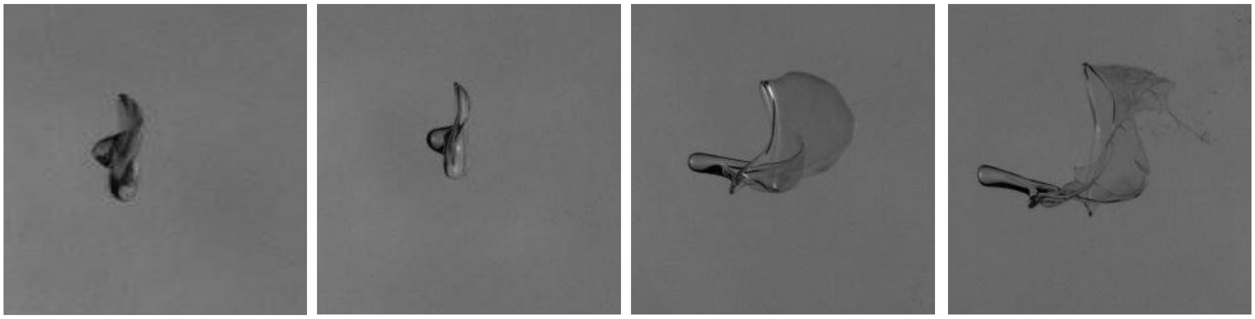

Figure 4.2 Shadowgraphs of drops undergoing aerodynamic fragmentation for $40 \leq We \leq 50$

As seen in figure 4.3, a peculiarity in droplet behavior begins at $We = 50$ where the droplet periphery forms wings that start to curve in toward the core. Under similar aerodynamic conditions, and for $Oh < 0.1$, the droplet exhibits sheet thinning mode where small fragments are stripped off from its periphery. However, in the current situation, the high drop viscosity resists stripping, and a small bag is formed downstream when the wings close together. The bag does undergo breakup, but the droplet core doesn't and is carried downstream.

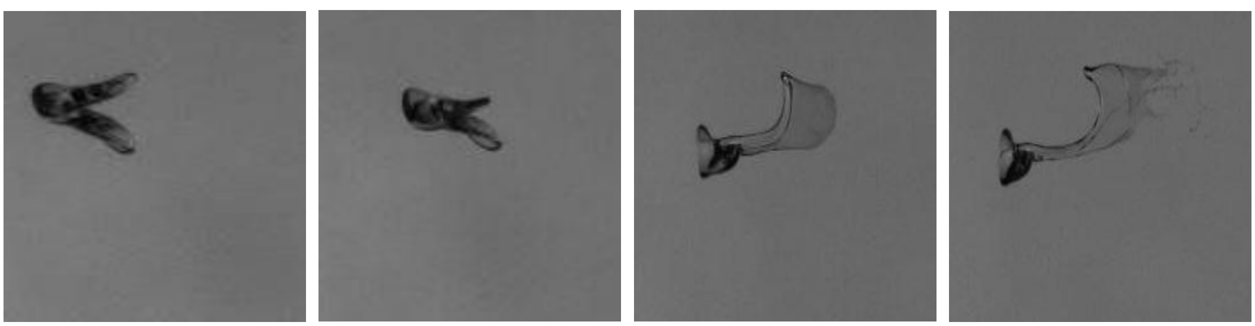

Figure 4.3 Shadowgraphs of drops undergoing aerodynamic fragmentation for $50 \leq We \leq 60$

As the aerodynamic force increases to $60 \leq We \leq 70$, the wings move into the wake region behind the drop core and merge (Figure 4.4). This reduces the area of the droplet exposed to aerodynamic shearing. The resulting dominance of surface tension prevents the breakup of the droplet. In fact, the second set of wings may form and repeat the process of flapping into the wake. Regardless, no breakup is observed. This behavior can be compared to the vibrational mode exhibited at low We by droplets of $Oh < 0.1$.

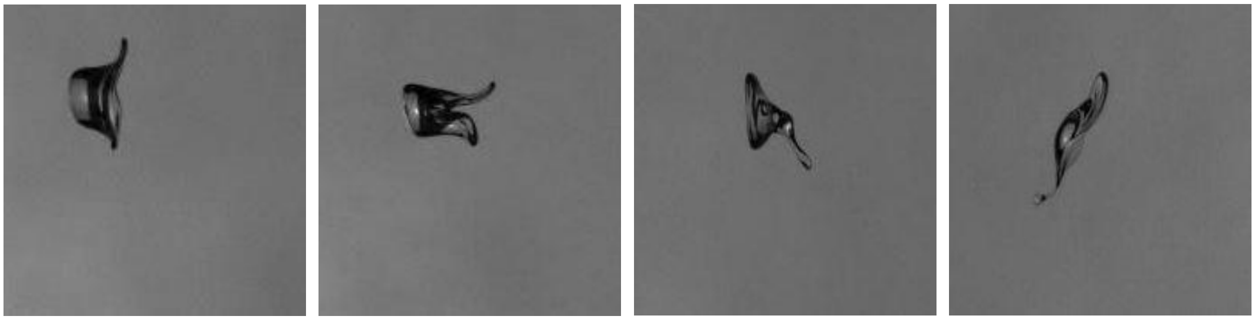

Figure 4.4 Shadowgraphs of drops undergoing aerodynamic deformation for $60 \leq We \leq 70$

Further increase in *We* causes the initial drop to form a bowl as shown in figure 4.5. Then, for $70 \leq We \leq 80$ the aerodynamic force is high enough to overcome the surface tension forces and a sequence of bags form and break apart. One is formed from the droplet core and is, therefore, larger in size. Additional bags form from the deformed original droplet periphery. Finally, the toroidal ring associated with the initial drop disintegrates. The toroidal ring, in this case, carries a much smaller fraction of the initial drop mass than its low *Oh* counterpart so its fragments are closer in size to those of the bags.

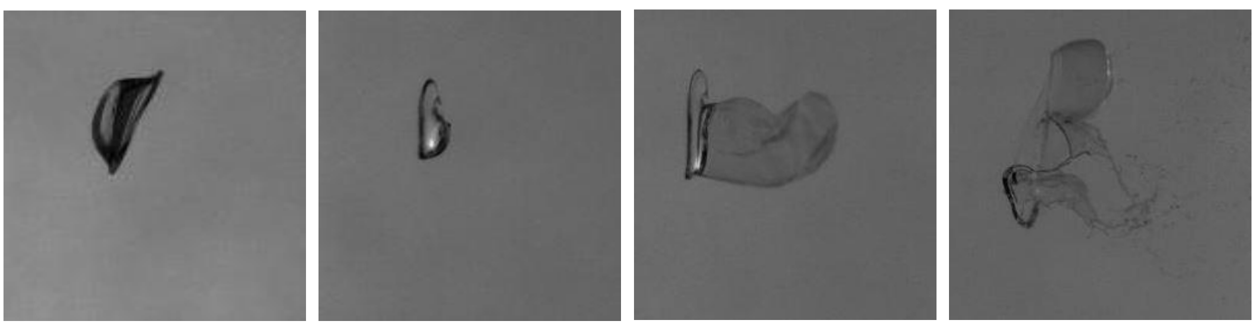

Figure 4.5 Shadowgraphs of drops undergoing aerodynamic fragmentation for $70 \leq We \leq 80$

An increase in *We* to $80 \leq We \leq 100$ leads to the near-simultaneous formation of multiple bags, with the bag formed from the core disintegrating before those formed from the periphery (figure 4.6). For $We \geq 100$, it can be seen in figure 4.7 that the formation and disintegration of bags from the core and periphery take place simultaneously. Hence the number of fragments formed from the secondary breakup is maximum in this case, and their sizes all lay in a single band.

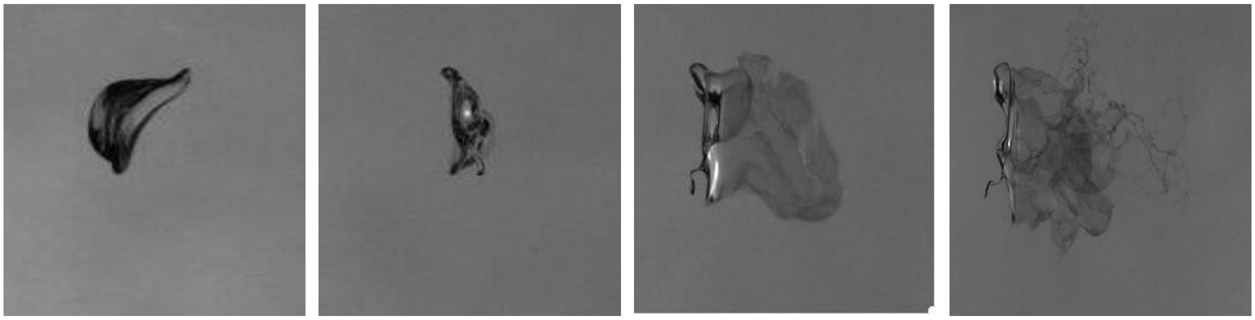

Figure 4.6 Shadowgraphs of drops undergoing aerodynamic fragmentation for $80 \le We \le 100$

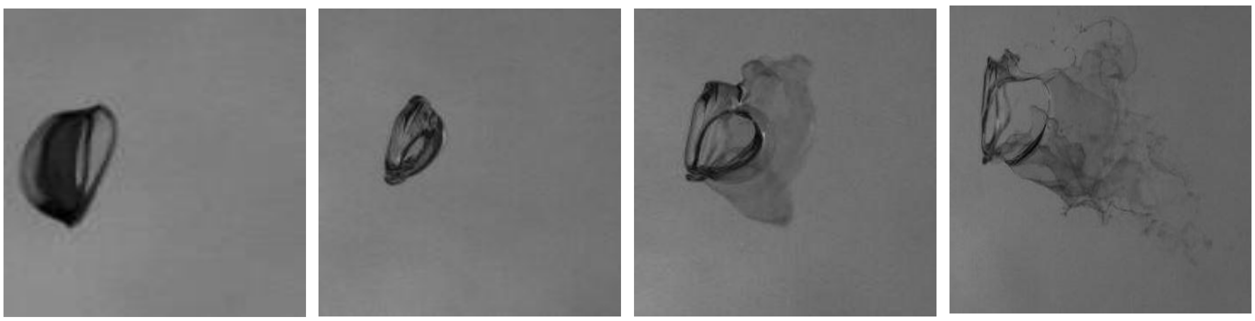

Figure 4.7 Shadowgraphs of drops undergoing aerodynamic fragmentation for $We \ge 100$

The results obtained above are in good agreement with Hsiang and Faeth (1994). However, the shear breakup wasn't observed up to *We* = 120. Rather, a regime with multiple bag formation took place. Further investigation at higher *We* are required to visualize sheet thinning breakup regime to the same level as reported here.

Finally, previous low *Oh* research has demonstrated that dome-shaped deformation leads to bag break up while bowl-shaped deformation leads to sheet thinning and catastrophic secondary atomization (Hsiang and Faeth,1994). For the current high *Oh* case, the transformation of the bowl to dome deformation causes the bag formation even at *We* as high as 120. This anomaly is of high relevance as it promotes bag breakup, thus enhancing the quality of atomization and could be important when forming sprays from high viscosity fuels or pharmaceutical compounds. Further studies were carried out using DIH to analyze the size and velocity distributions of fragments formed from in the various regimes.

4.2 Digital in-line Holography

4.2.1 Size volume *pdfs*

Digital in-line Holography (DIH) was used to develop size-velocity *pdfs* for droplet atomization. A collimated laser illuminates the object field and the resulting diffraction pattern is digitally recorded. Numerical reconstruction of the volumetric field is performed via the solution of the diffraction integral equations (Schnars and Jueptner 2005; Katz and Sheng 2010). DIH was carried out for a range of Weber numbers, $35 < We < 120$. An experiment was conducted for two sets of Ohnesorge numbers, *Oh* = 0.5 and *Oh* = 1. Size-volume pdfs for *Oh* = 1 are discussed below.

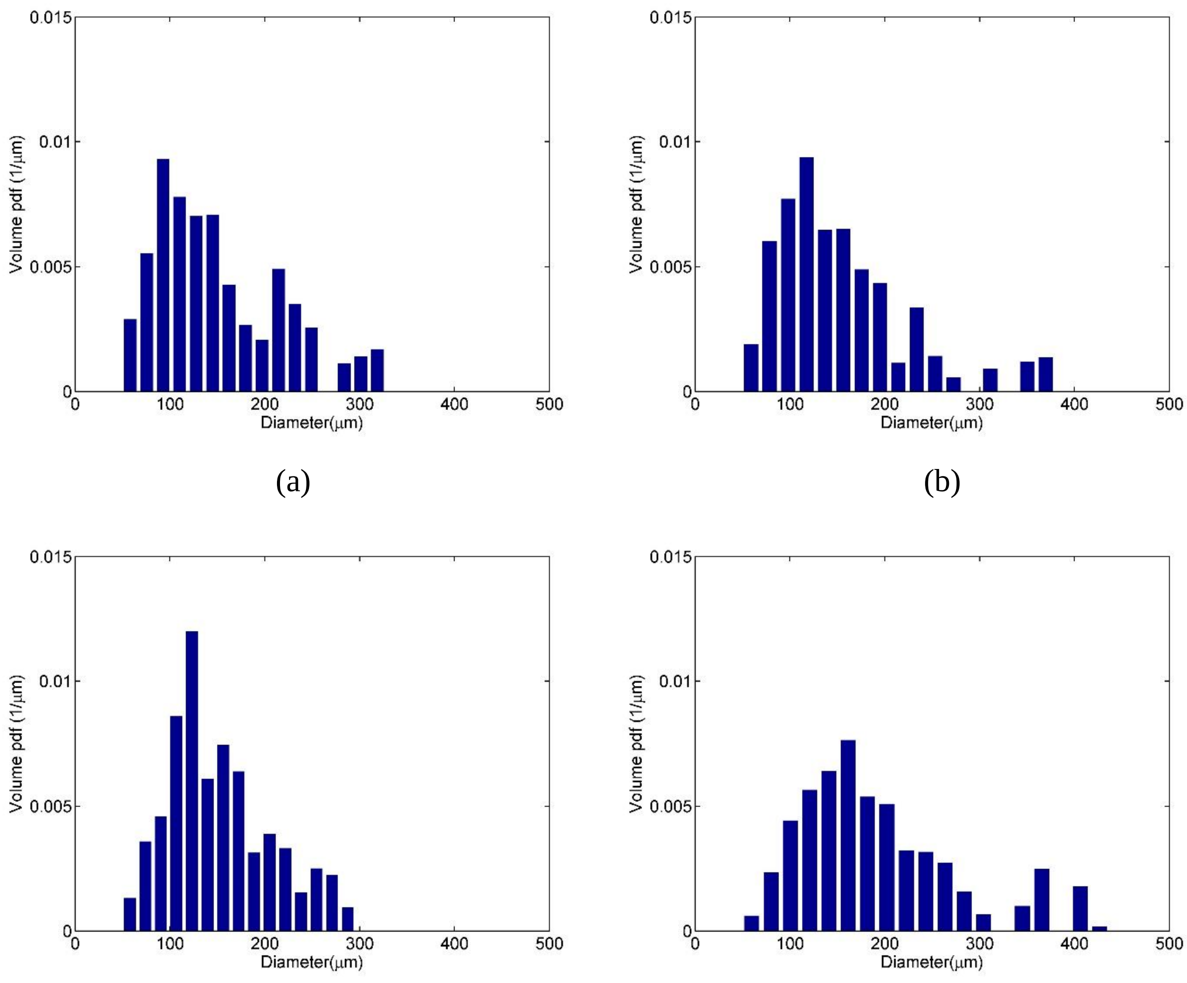

(a) (b)

(c) (d)

Figure 4.8 Fragment size-volume *pdf* of (V,d) for drop breakup at *Oh* = 1, *We* = 35 a) $\tau_1 = 0.36$, b) $\tau_2 = 0.58$ c) $\tau_3 = 0.87$ d) $\tau_4 = 1.10$

From the size *pdfs* presented above, it is evident that for lower Weber numbers i.e. *We* = 35, the distribution peak shifts towards the right as time increases. This means that the size of the droplets increases as time increases which is consistent with the results obtained in section 4.1. As the bag ruptures, it produces droplets in a wide range of sizes. This is due to the high viscosity of the droplets. The viscosity is high enough to overcome the aerodynamic forces and hence produce a good amount of large size droplets. At τ_4 there is a significant peak in droplets with a diameter between 300 µm and 400 µm. This is due to the contribution from the toroidal ring break up. The rim consists of the droplet core and the secondary droplets stripping out from the rim are of large sizes. Additionally, it is also noted that the peak reduces as time increases as the droplet core is contained in the toroidal ring for, *We* = 35.

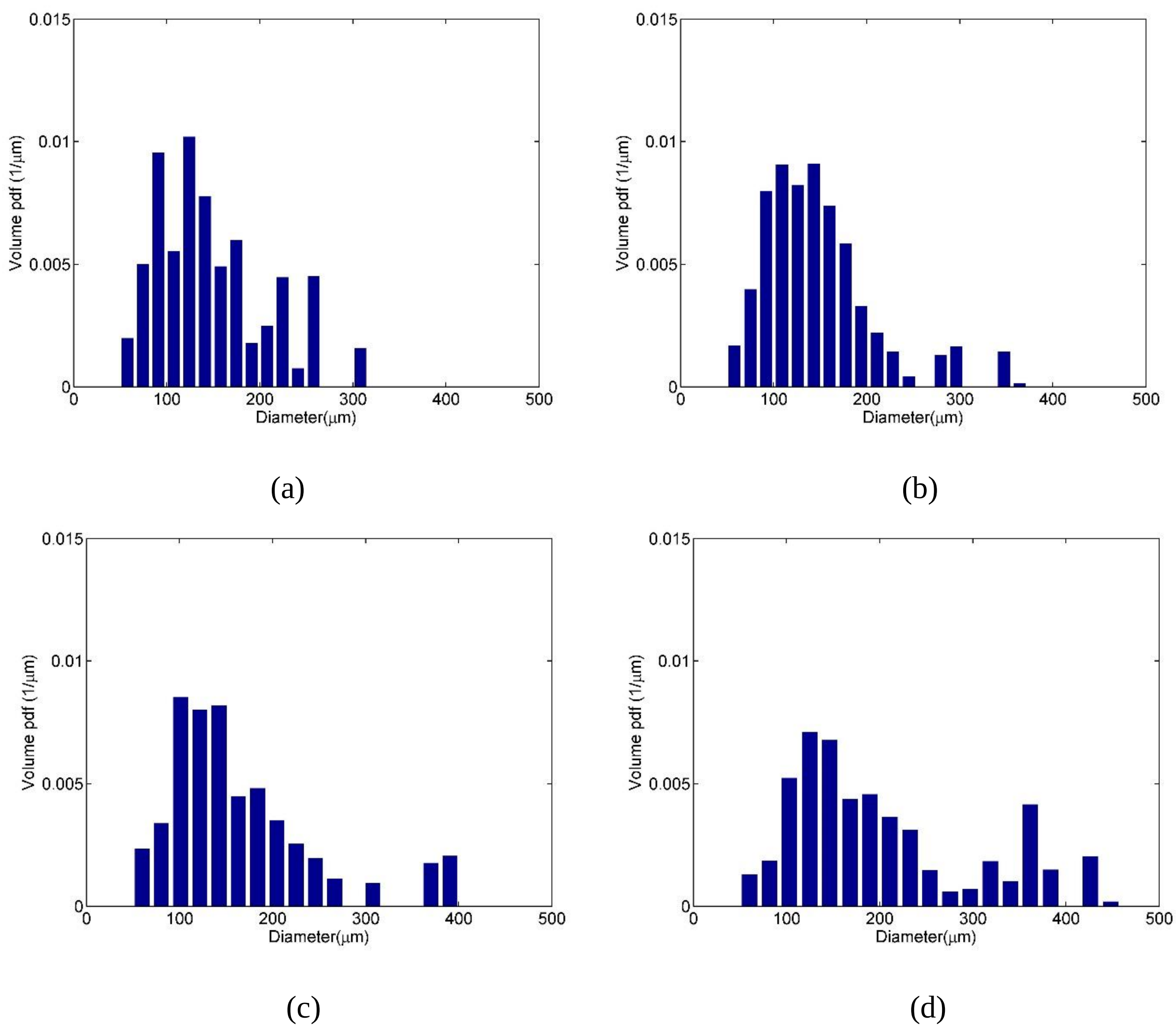

(a) (b)

(c) (d)

Figure 4.9 Fragment size-volume *pdf* of (V,d) for drop breakup at *Oh* = 1, *We* = 45 a) τ_1 = 0.38, b) τ_2 = 0.62 c) τ_3 = 0.98 d) τ_4 = 1.22

As the breakup mode translates from bag to multimode a similar trend can be seen in size distribution. As the bag ruptures, it contributes to the highest percentage of small droplets at τ_1. The distribution peak falls from τ_1 to τ_4 as the core of the droplet is contained in the stamen. The bi-modal distribution at τ_4 is significant at *We* = 45 as the drop core containing stamen disintegrates itself due to aerodynamic shearing.

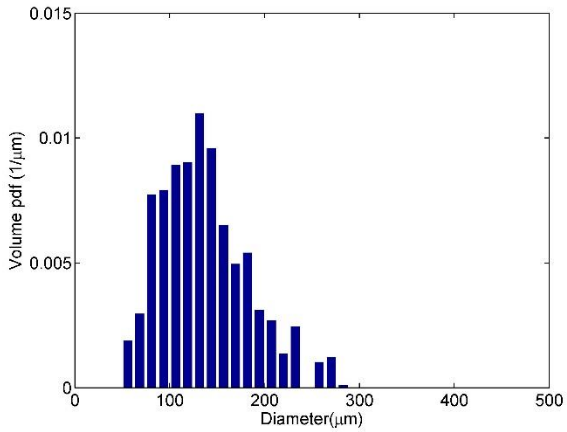

(a)

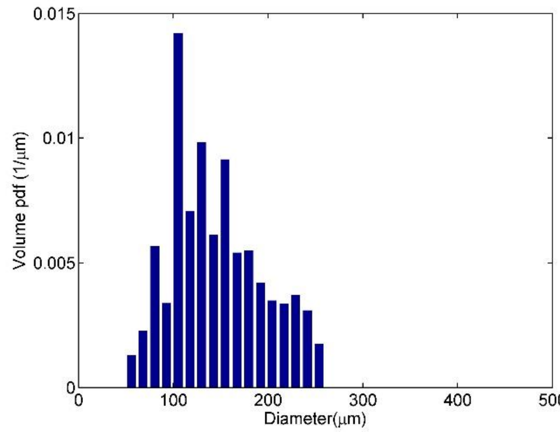

(b)

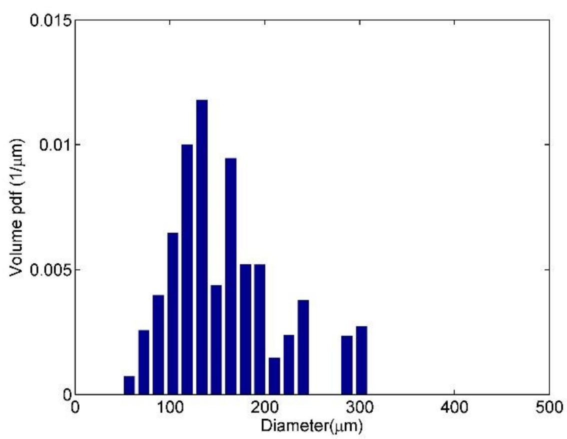

(c)

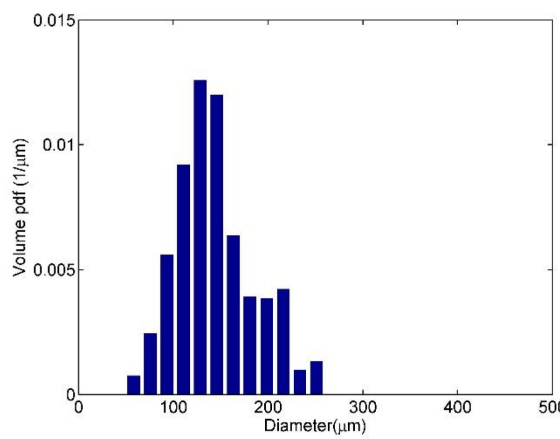

(d)

Figure 4.10 Fragment size-volume *pdf* of (V,d) for drop breakup at *Oh* = 1, *We* = 80 a) τ_1 = 0.37, b) τ_2 = 0.68 c) τ_3 = 0.98 d) τ_4 = 1.30

Figure 4.10 shows the pdfs for multiple bag break up at different time steps. It is seen that the peak increases with time. This is because of the dominance of the disruptive forces over surface tension and viscous effects. At τ_2, distribution peak is at its maximum. This when all the bags disintegrate into smaller secondary drops. At τ_3 a decent number of large droplets can be seen as a result of rim breakup. However, in this case, the droplet core is within the bags and the droplets formed from rim breakup break apart immediately. This justifies the size distribution shown at τ_4 where a unimodal distribution can be seen. The size of the majority of the droplets lies between 110 and 160 μm with the large droplets missing unlike in the lower *We* regime.

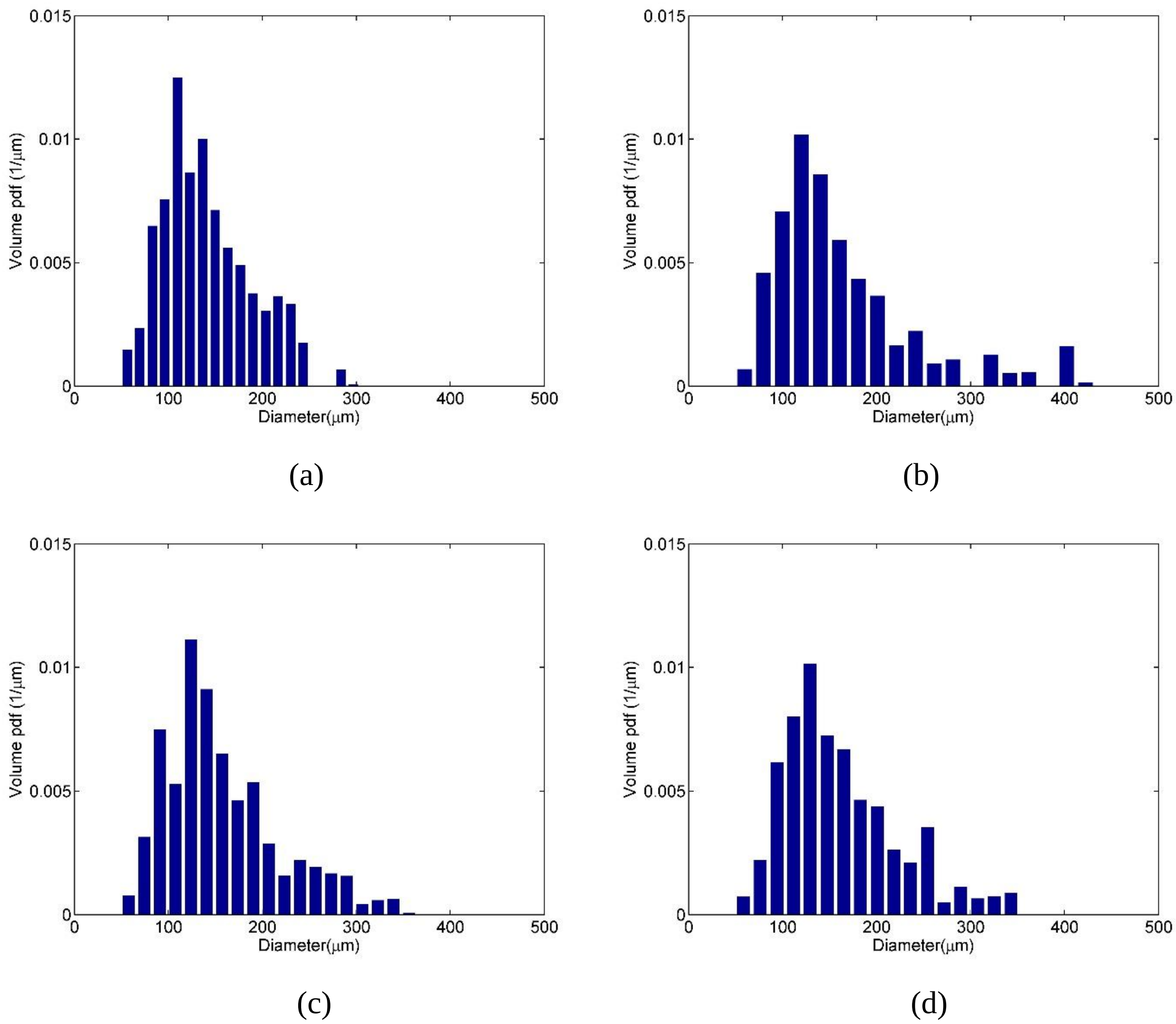

Figure 4.11. Fragment size-volume *pdf* of (V,d) for drop breakup at *Oh* = 1, *We* = 90 a) $\tau_1 = 0.42$, b) $\tau_2 = 0.69$ c) $\tau_3 = 1.07$ d) $\tau_4 = 1.37$

For the above case, the maximum peak is at τ_1, which is a depiction of large aerodynamic forces leading to the secondary breakup. The peak decreases from τ_1 to τ_4. Again, a certain number of large drops can be seen at τ_2 which eventually shatters to contribute to a more uniform distribution at successive time intervals.

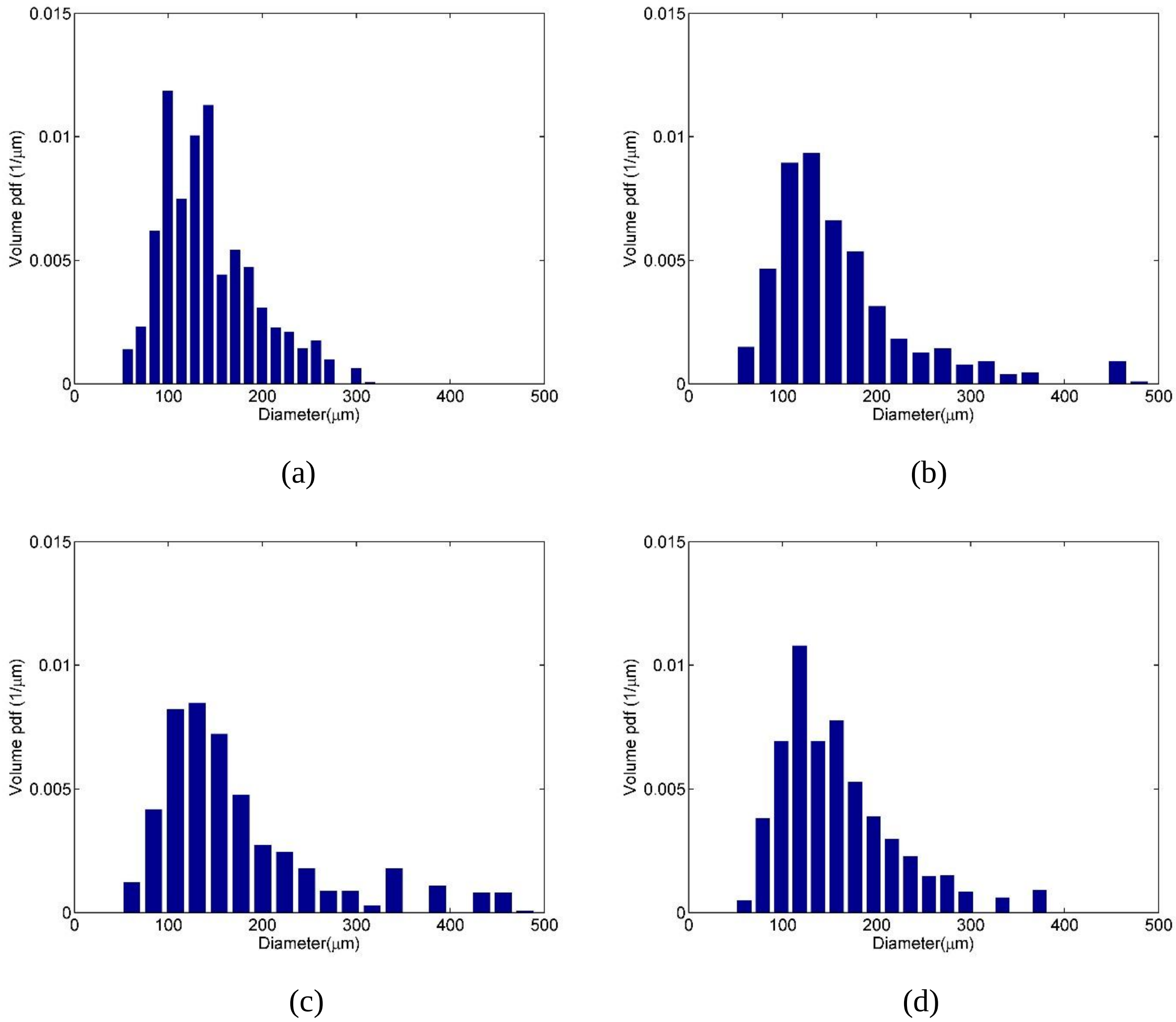

Figure 4.12. Fragment size-volume *pdf* of (V,d) for drop breakup at *Oh* = 1, *We* = 120 a) τ_1 = 0.44, b) τ_2 = 0.72 c) τ_3 = 1.12 d) τ_4 = 1.43

At *We* = 120, a dominant peak is depicted in the pdf plot at τ_1. Air velocities are high enough to produce droplet breakup. Multiple bags are formed at this *We* as can be seen in section 4.1. However, the strong aerodynamic forces atomize the droplet into fine secondary droplets and are shown in figure 4.12 (a). Also, as time increases, the large diameter droplets seen at τ_2 and τ_3 breaks into smaller droplets to form a prominent peak of drops with110 μm diameter. From the above results, it is noted that as *We* increases the distribution peak tends to form at τ_1. This is majorly due to the increasing aerodynamic forces that causes relatively faster breakup.

To provide a stronger validation for the results presented above, DIH was carried out for droplets of *Oh* = 0.5. Size-volume pdfs for *Oh* = 0.5 are discussed here.

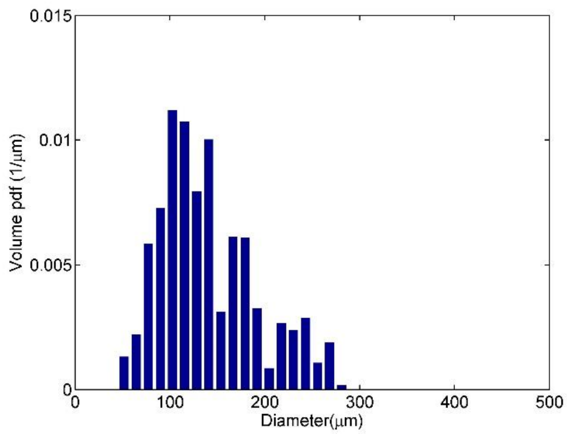

(a)

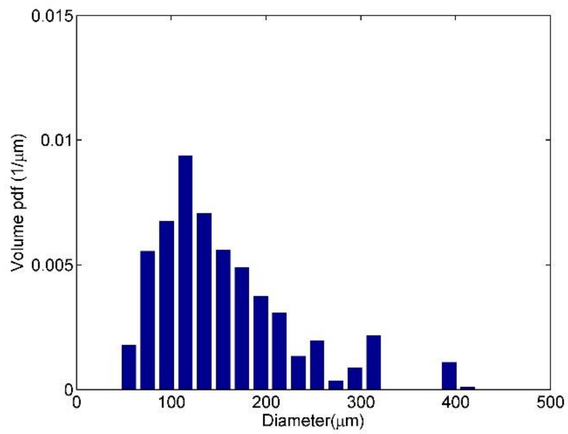

(b)

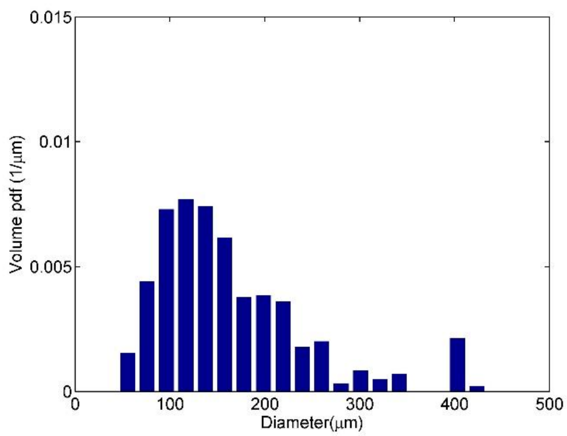

(c)

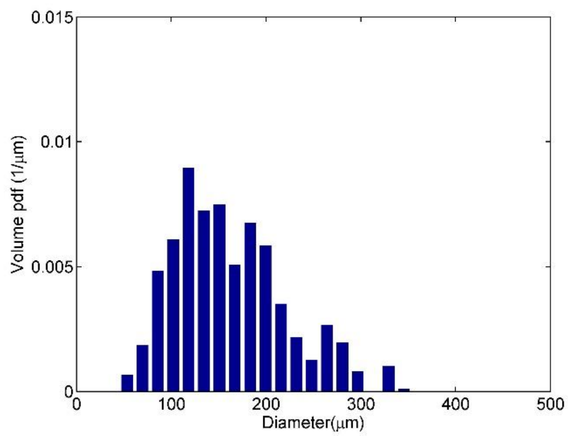

(d)

Figure 4.13 Fragment size-volume *pdf* of (V,d) for drop breakup at *Oh* = 0.5, *We* = 40 a) τ_1 = 0.34, b) τ_2 = 0.55 c) τ_3 = 0.80 d) τ_4 = 0.97

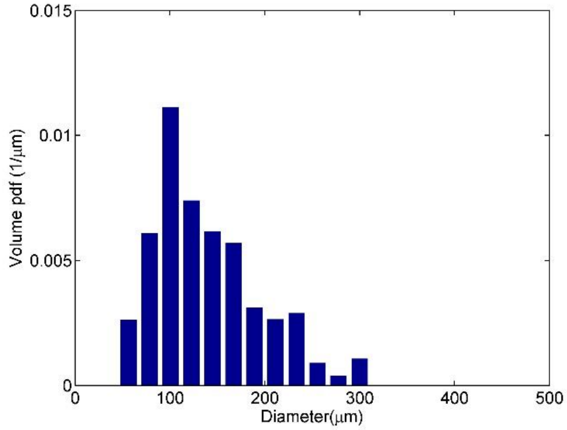

(a)

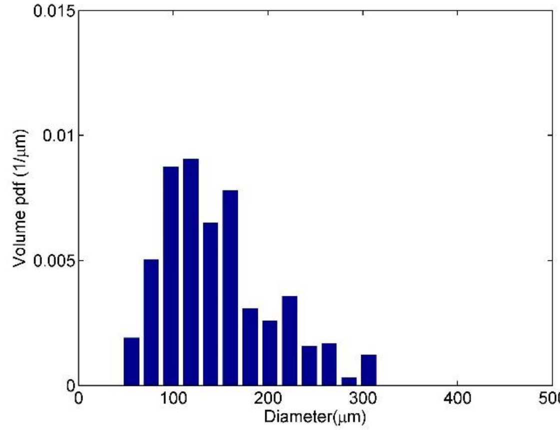

(b)

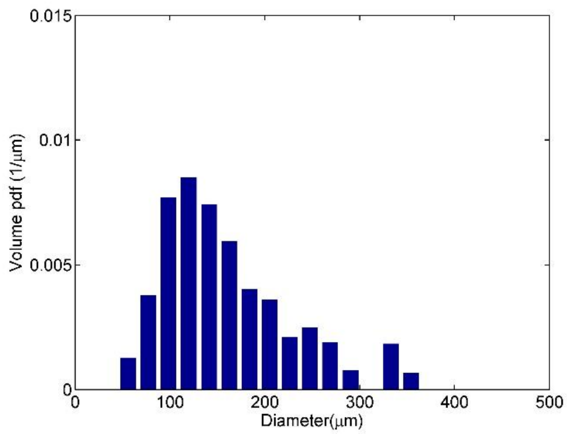

(c)

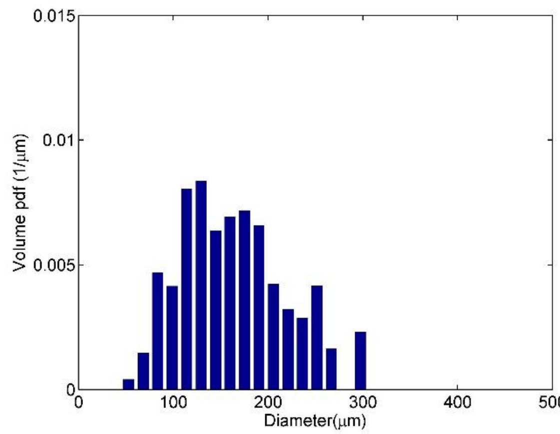

(d)

Figure 4.14 Fragment size-volume *pdf* of (V,d) for drop breakup at *Oh* = 0.5, *We* = 60 a) τ_1 = 0.36, b) τ_2 = 0.60 c) τ_3 = 0.91 d) τ_4 = 1.01

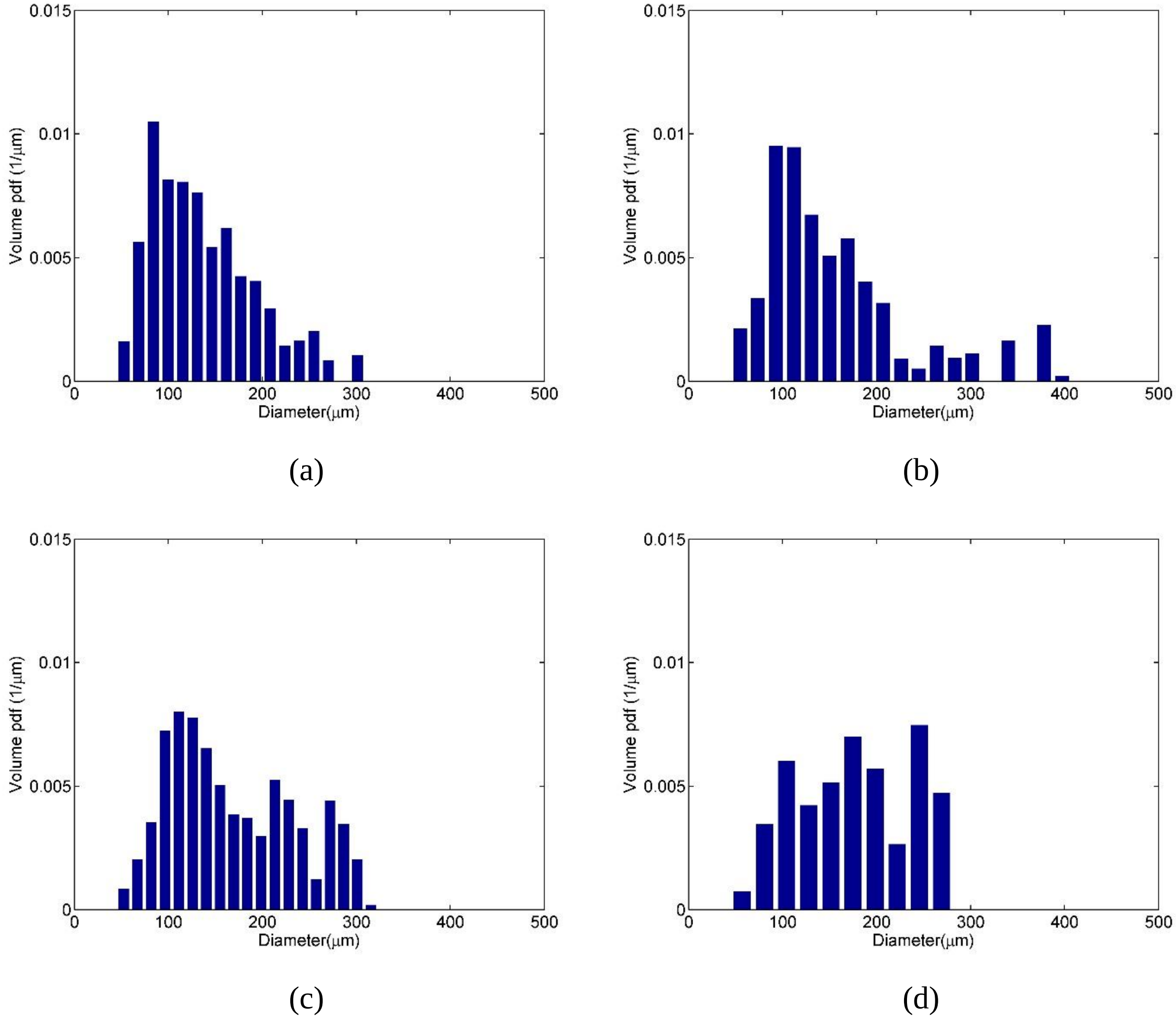

Figure 4.15 Fragment size-volume *pdf* of (V,d) for drop breakup at *Oh* = 0.5, *We* = 80 a) τ_1 = 0.38, b) τ_2 = 0.64 c) τ_3 = 0.92 d) τ_4 = 1.04

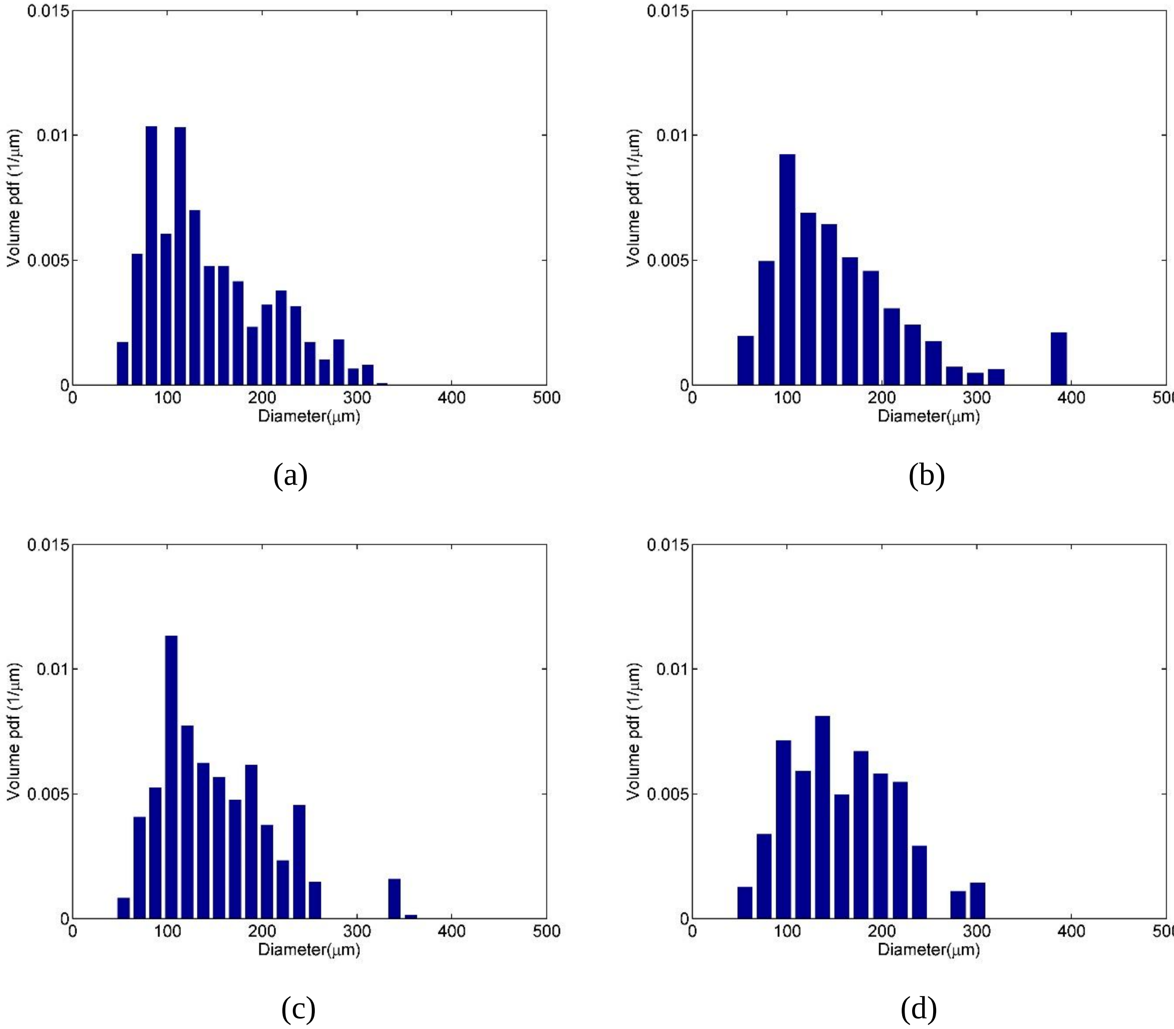

Figure 4.16 Fragment size-volume *pdf* of (V,d) for drop breakup at *Oh* = 0.5, *We* = 90 a) τ_1 = 0.42, b) τ_2 = 0.67 c) τ_3 = 1.02 d) τ_4 = 1.15

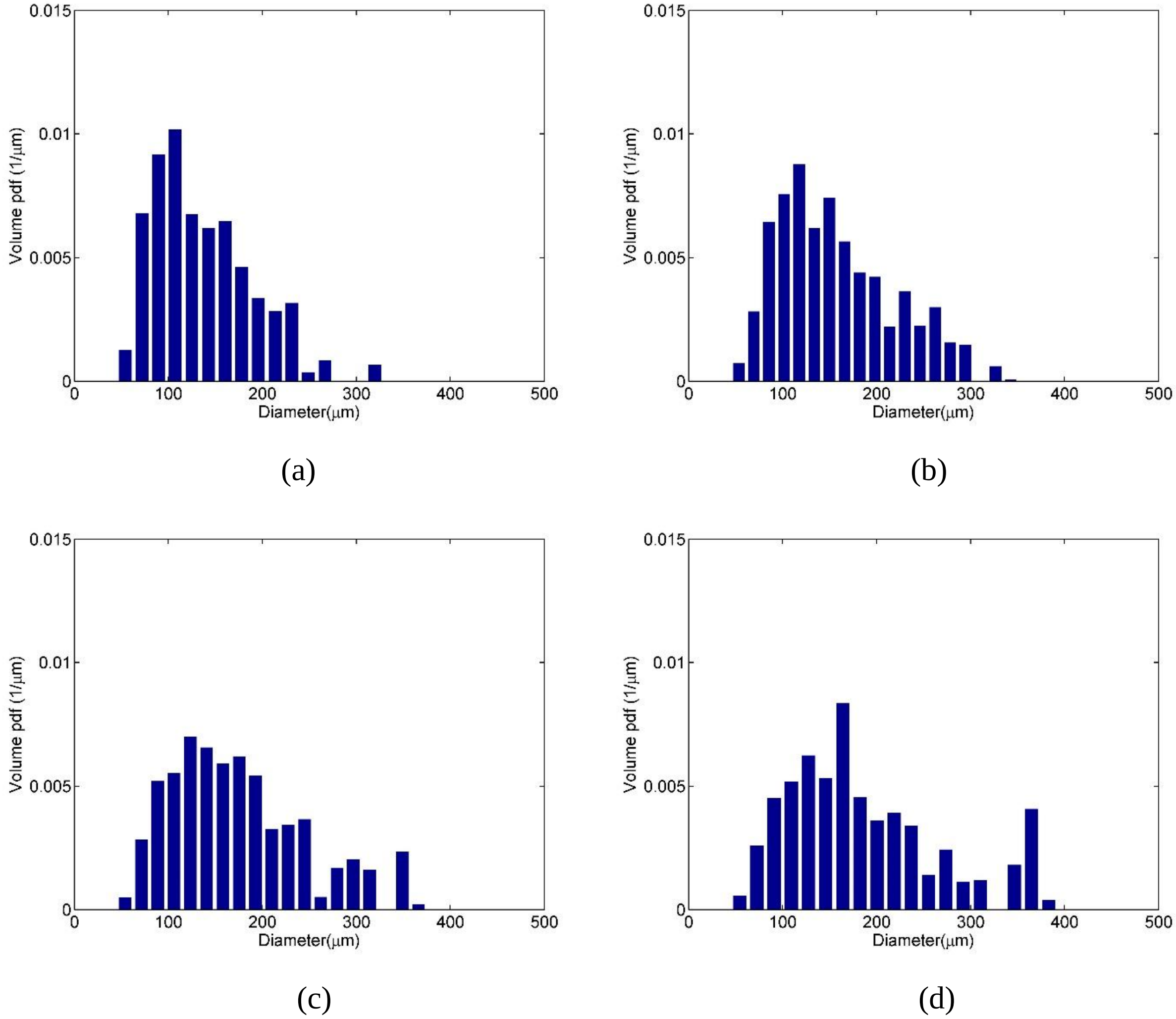

Figure 4.17 Fragment size-volume *pdf* of (V,d) for drop breakup at *Oh* = 0.5, *We* = 100 a) τ_1 = 0.44, b) τ_2 = 0.64 c) τ_3 = 1.12 d) τ_4 = 1.30

From the results presented for *Oh* = 0.5, it is evident that the *pdfs* represent a trend similar to that of *Oh* = 1. However, at high Weber numbers at τ_4, an evident number of large size droplets are present. This is primarily due to the lower viscosity of the droplet. At Weber numbers 80, 90 and 100 the rim in multiple bag break up contributes to larger sized drops. This could also be due to the time step at which the *pdfs* are evaluated. In this case, the moment at which τ_4 is evaluated is lower than that for *Oh* = 0.1. Therefore, with an increase in time, the ligaments from the weak toroidal ring will disintegrate into smaller droplets.

4.2.2 Velocity *pdfs*

Velocity *pdf*s were created for the same range of Weber numbers by tracking particles in two consecutive holograms at selected times after the start of breakup. Two values of Ohnesorge numbers have been considered to obtain a better understanding of the droplet velocity distribution.

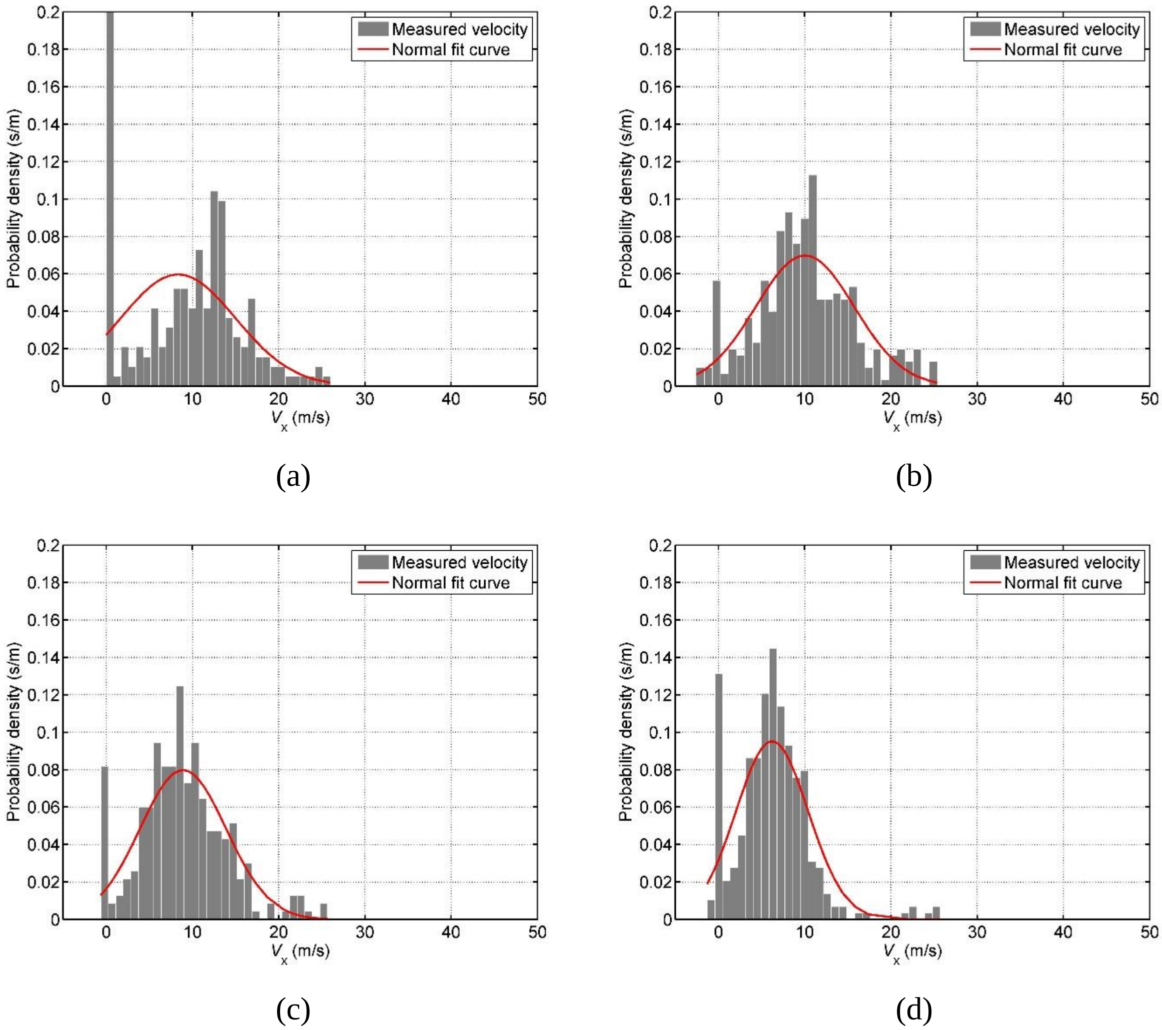

Figure 4.18 Fragment Velocity *pdf* of (v) for drop breakup at *Oh* = 1, *We* = 35 a) τ_1 = 0.36, b) τ_2 = 0.58 c) τ_3 = 0.87 d) τ_4 = 1.10

From figure 4.18, the velocity development over time can be seen. At τ_1, the bag just begins to rupture and there is a relatively smaller number of droplets to track leading to a higher density at $V_x = 0$. However, small droplets formed from bag breakup initiate at a velocity of 7 m/s. As the time increases more secondary drops are formed and accelerate to a velocity close to 10 m/s. However, at τ_4 the droplets begin to decelerate and hence the distribution peak is at a lower velocity of 6 m/s. Additionally, at τ_4 maximum droplets move out of frame and there is a huge contribution from the rim leading to the zero-velocity density distribution.

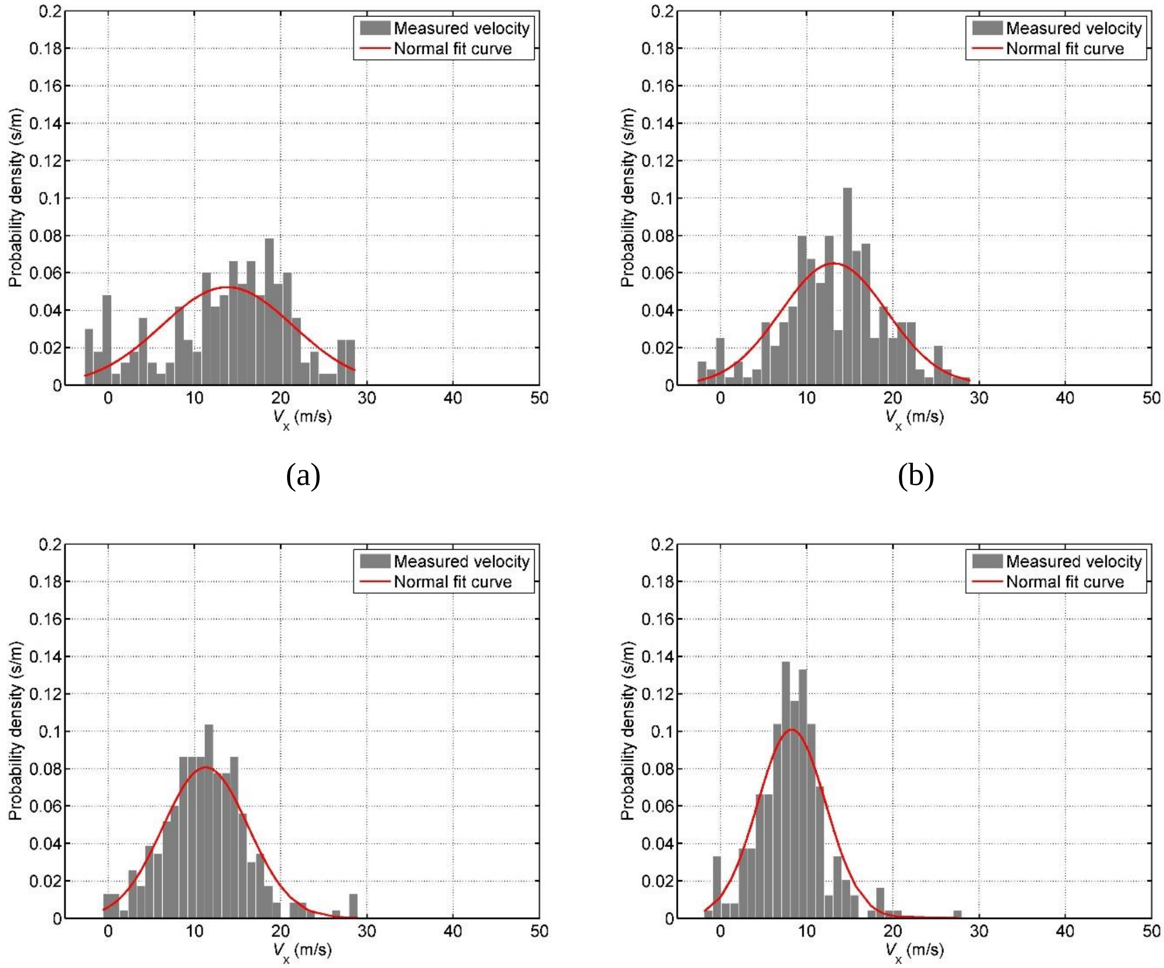

(a) (b)

(c) (d)

Fig 4.19 Fragment Velocity *pdf* of (v) for drop breakup at *Oh* = 1, *We* = 45 a) τ_1 = 0.38, b) τ_2 = 0.62 c) τ_3 = 0.98 d) τ_4 = 1.22

As Weber number increases, the break up process fastens. For *We* = 35, the droplets initially have a velocity close to 15 m/s and the decelerates to 9 m/s as time progresses. The distribution begins to narrow down as time increases as more droplets tend to attain a stable velocity.

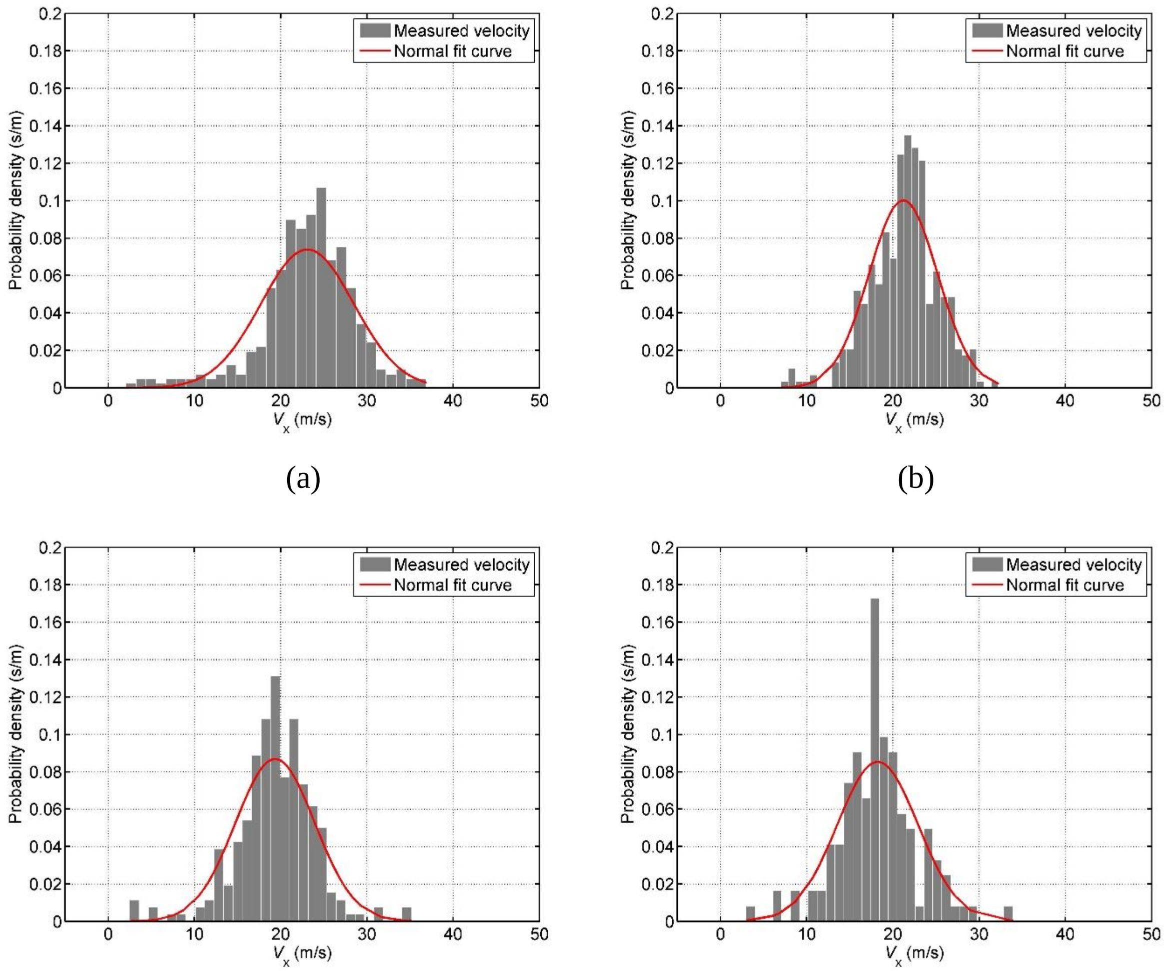

(a) (b)

(c) (d)

Figure 4.20 Fragment Velocity *pdf* of (v) for drop breakup at *Oh* = 1, *We* = 80 a) τ_1 = 0.37, b) τ_2 = 0.68 c) τ_3 = 0.98 d) τ_4 = 1.30

With further increase in Weber number, the atomization of droplet increases. It is seen that more particles attain a stable Velocity at τ_1 compared to previous cases. However, a different trend is represented at higher *We*. The peak shifts to the right from τ_1 to τ_2 depicting droplet acceleration and then shifts to left as time progresses. The secondary drops are small enough to accelerate in the flow and hence attain greater velocity with an increase in time. Also, the peak drops down and the distribution widens with time. The dominant aerodynamic forces lead to the breakup of the rim in the multiple bag breakup mode forming droplets in a range of sizes and velocities. The distribution peaks at 21 m/s and shifts to 19 m/s as droplet decelerates.

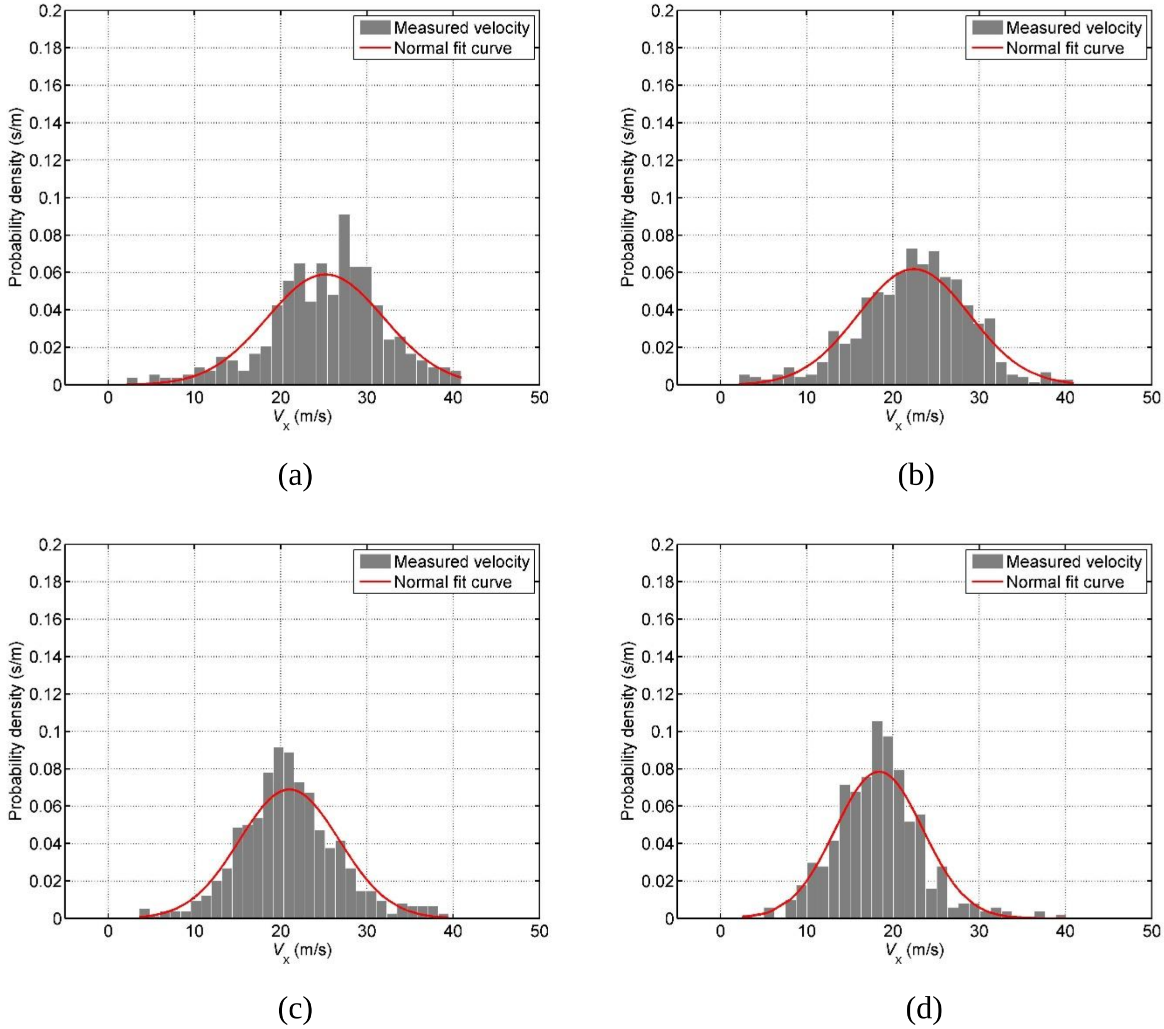

Figure 4.21 Fragment Velocity *pdf* of (v) for drop breakup at *Oh* = 1, *We* = 90 a) τ_1 = 0.42, b) τ_2 = 0.69 c) τ_3 = 1.07 d) τ_4 = 1.37

At *We* = 90, a trend similar to *We* = 80 is observed. The distribution widens with an increase in time and from τ_1 to τ_2 where secondary breakup occurs increasing the number of droplets. However, as time increases further, distribution peaks at 21 m/s. As droplets slow down, the distribution peak shifts to the left to settle at 20 m/s.

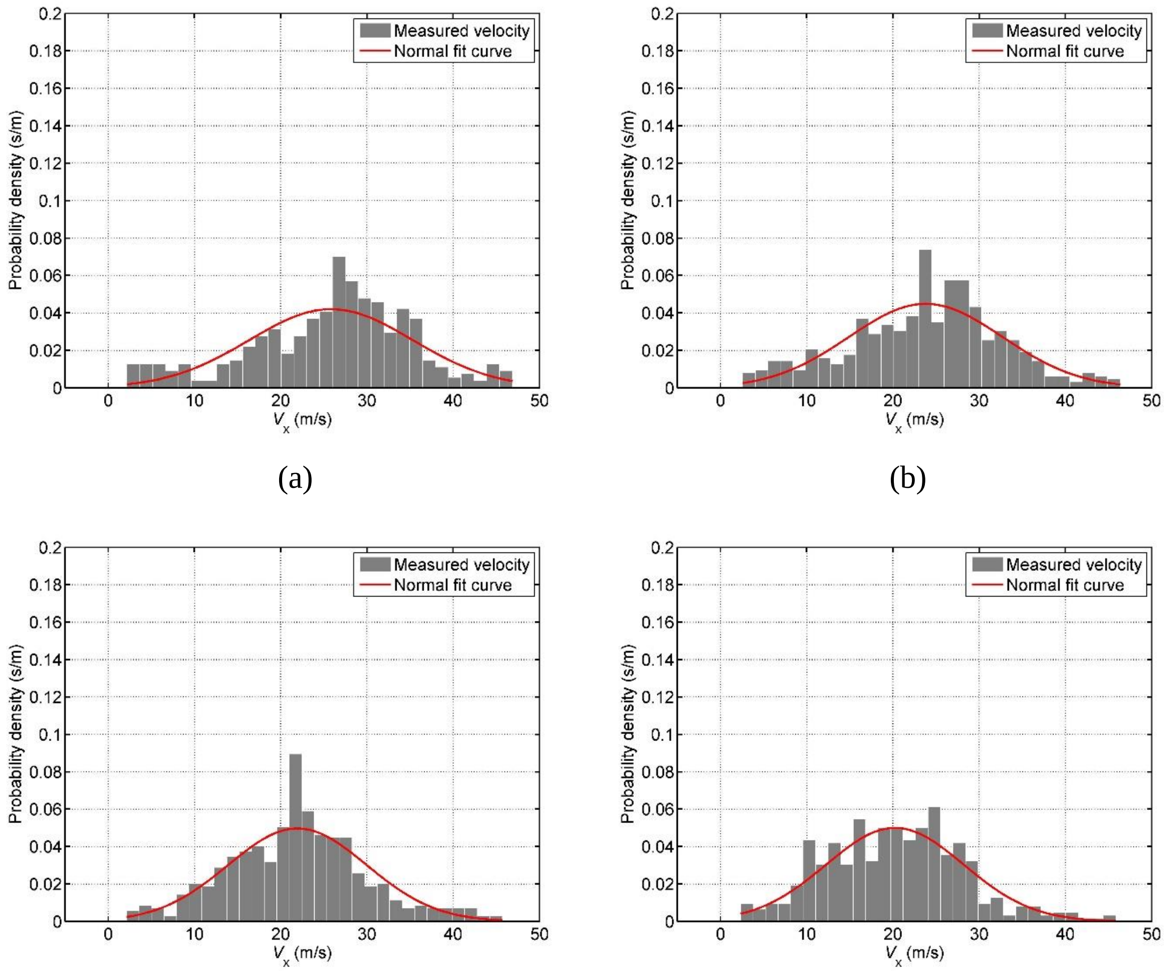

(a) (b)

(c) (d)

Figure 4.22 Fragment Velocity *pdf* of (v) for drop breakup at *Oh* = 1, *We* = 120 a) τ_1 = 0.44, b) τ_2 = 0.72 c) τ_3 = 1.12 d) τ_4 = 1.43

At *We* = 120 the distribution width appears to remain the same with time. This is majorly due to the high air velocity. The strong aerodynamic forces initiate the breakup of the bag quickly and secondary atomization occurs faster. This leads to a constant distribution of droplet sizes over time. However, a shift in pdf peak is seen from τ_1 to τ_4 as the droplets slow down.

Velocity pdfs were constructed for *Oh* = 0.5. The results obtained are presented below to support the velocity trends previously obtained.

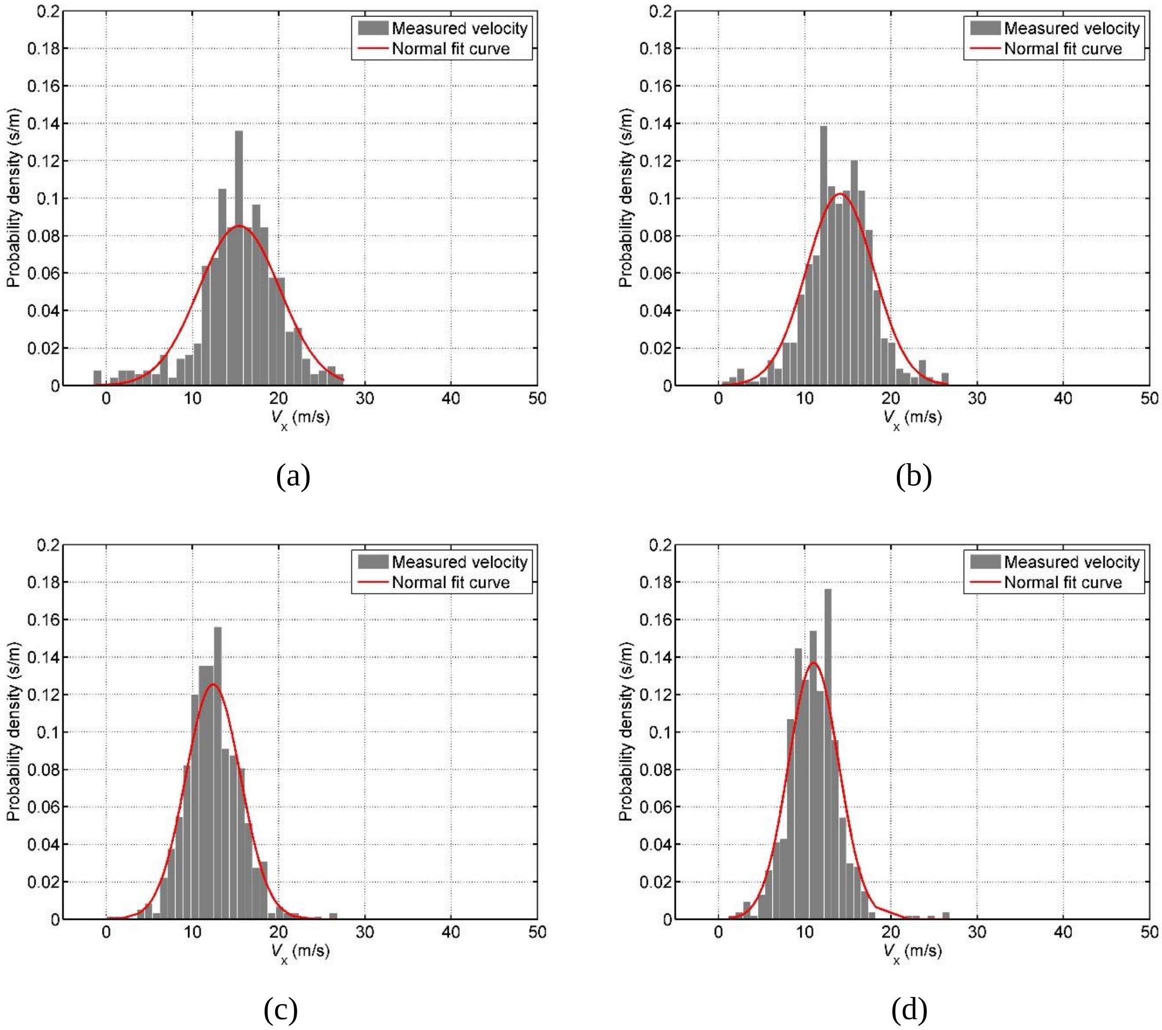

Figure 4.23 Fragment Velocity *pdf* of (v) for drop breakup at *Oh* = 0.5, *We* = 40 a) τ_1 = 0.34, b) τ_2 = 0.55 c) τ_3 = 0.80 d) τ_4 = 0.97

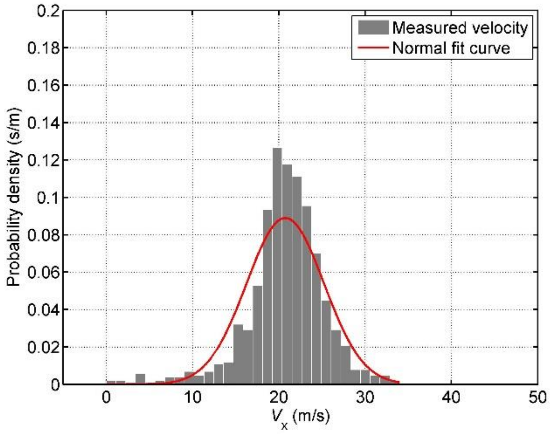

(a)

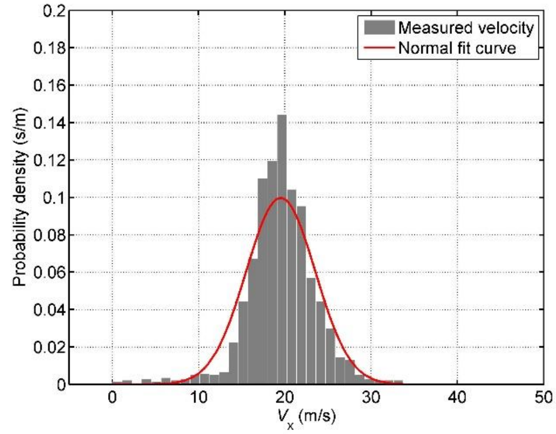

(b)

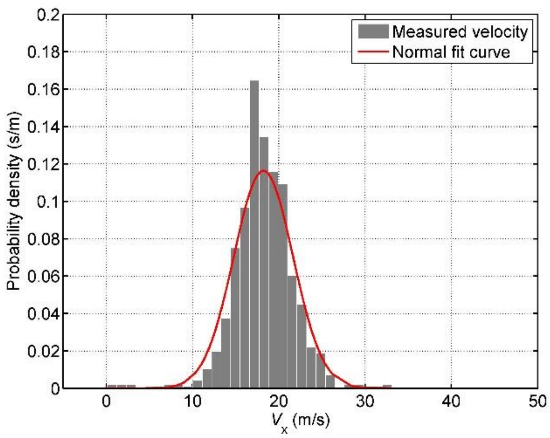

(c)

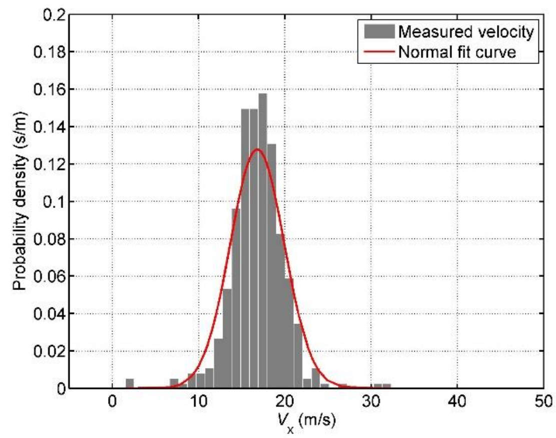

(d)

Figure 4.24 Fragment Velocity *pdf* of (v) for drop breakup at *Oh* = 0.5, *We* = 60 a) τ_1 = 0.36, b) τ_2 = 0.60 c) τ_3 = 0.91 d) τ_4 = 1.01

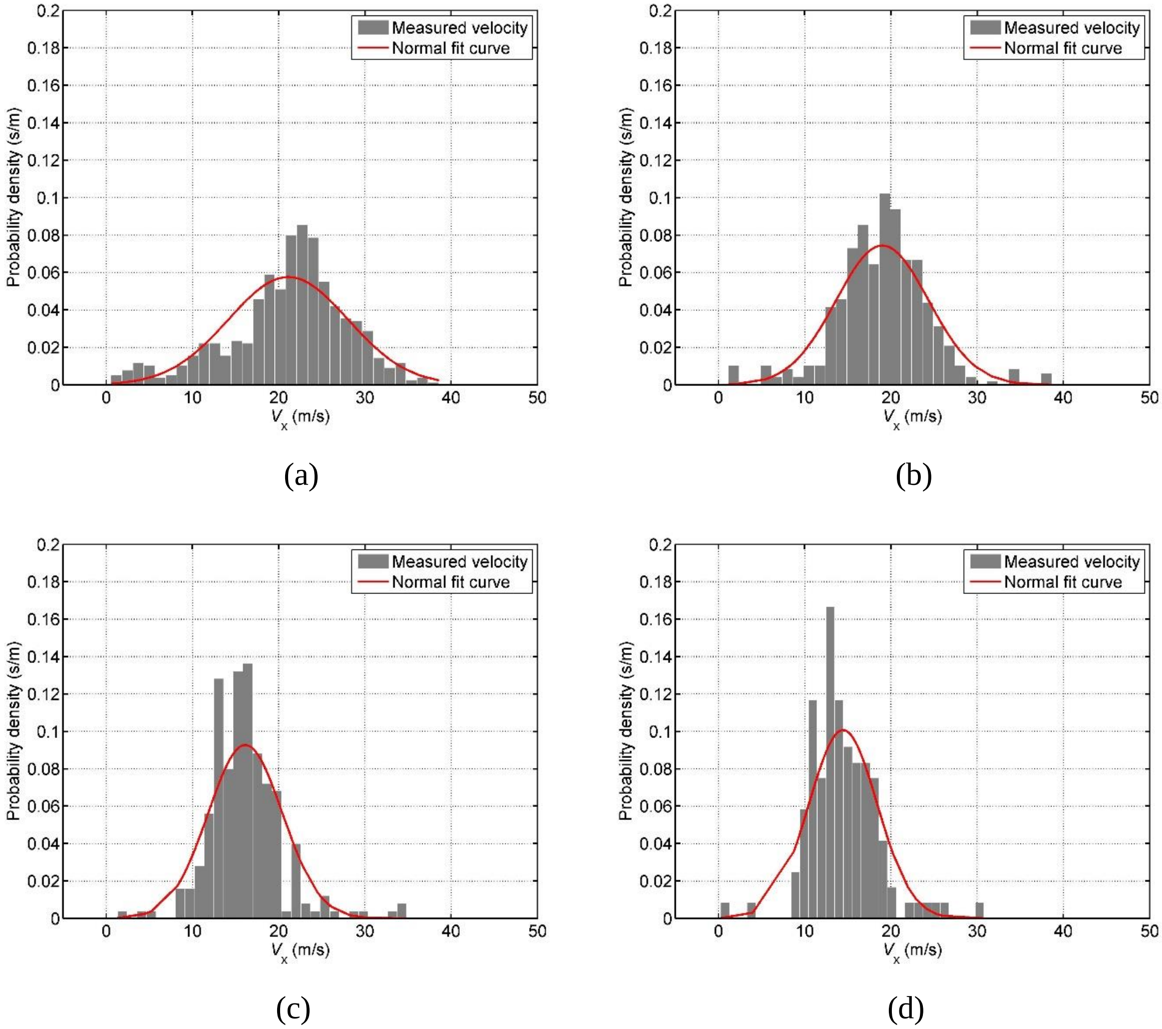

Figure 4.25 Fragment Velocity *pdf* of (v) for drop breakup at *Oh* = 0.5, *We* = 80 a) τ_1 = 0.38, b) τ_2 = 0.64 c) τ_3 = 0.92 d) τ_4 = 1.04

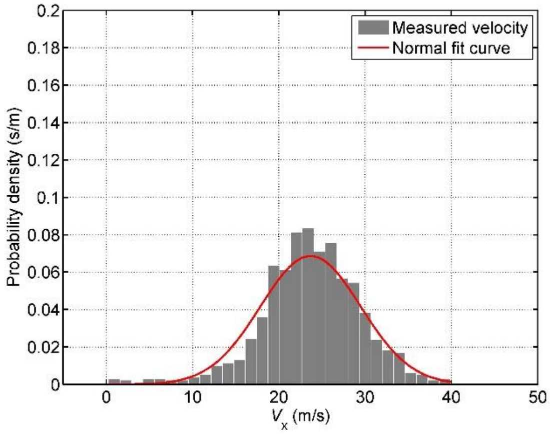

(a)

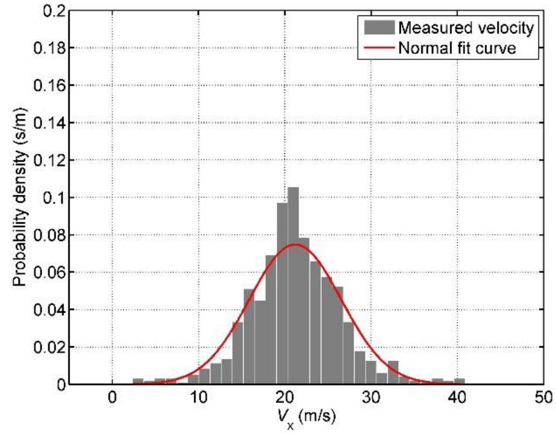

(b)

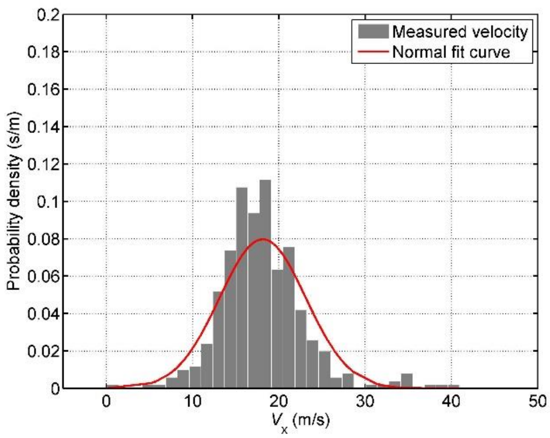

(c)

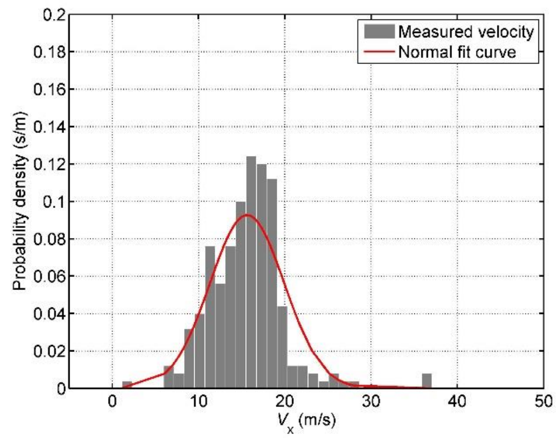

(d)

Figure 4.26 Fragment Velocity *pdf* of (v) for drop breakup at at *Oh* = 0.5, *We* = 90 a) τ_1 = 0.42, b) τ_2 = 0.67 c) τ_3 = 1.02 d) τ_4 = 1.15

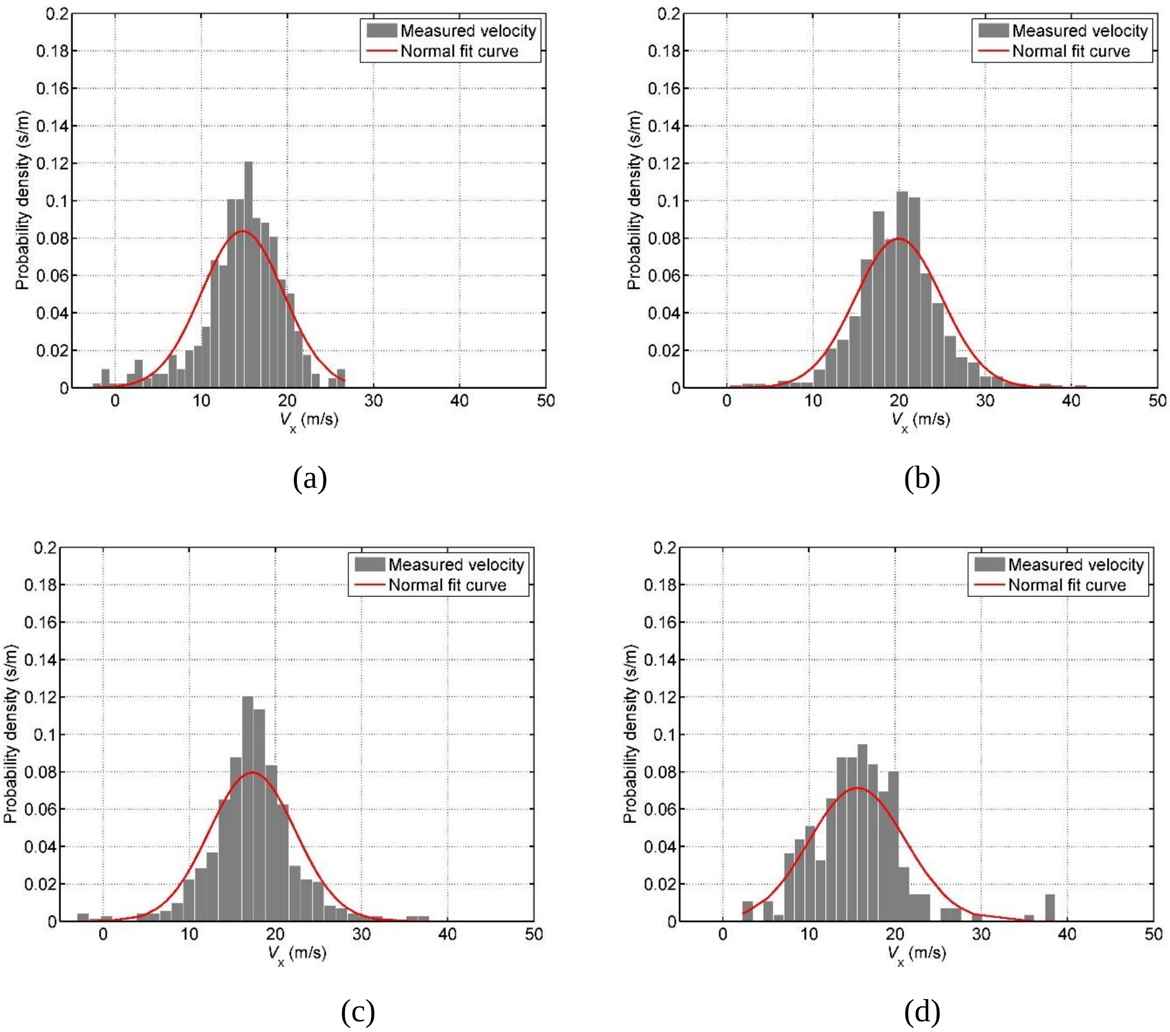

Figure 4.27 Fragment Velocity *pdf* of (v) for drop breakup at *Oh* = 0.5, *We* = 100 a) τ_1 = 0.44, b) τ_2 = 0.64 c) τ_3 = 1.12 d) τ_4 = 1.30

For *Oh* = 0.5, with an increase in *We*ber number, trends are similar to that of *Oh* = 1. The only difference to be noted is the width of the distribution. Here, the viscosity is much lower than the previous case. Hence, the droplet breakup at earlier time intervals and secondary drops produced are greater in number. This leads to a wider distribution at the time of breakup.

4.3 Particle Image Velocimetry

Section 4.1 describes a unique case of droplet deformation at $60 \leq We \leq 70$ where no breakup occurs. PIV was carried out to study the aerodynamic effect for this case. Results obtained for *We* = 60 and *We* = 80 are presented below.

Temporal history of the air flow field around the deforming droplet was attained by implementing a time delay to the triggering system. 800 PIV realizations were carried out and most repeating droplet behavior was selected. Image pairs exhibiting this deformation were averaged to obtain velocity and vortex contours for the flow field. The experiment was repeated for various delay times to obtain the droplet at different time instants. Results are presented for three delay times and the time gap between data sets is 0.5-1m/s. PIV image pairs are processed using the LaVision DaVis v8 software. An adaptive correlation with 25% overlap is performed. This PIV deconvolution technique begins with interrogation windows of 128 128 pixels, performs two refinement steps, and leads to a final vector field corresponding to interrogation areas of 32 32 pixels (A.K. Flock e*t al*., 2012). Unrealistic data is filtered out by setting a moving average filter that allows a maximum velocity change of 10% within a 3x3 interrogation window. This ensures that only valid velocity vectors are retained, and any inaccurate data is removed. Finally, a droplet from the raw image is overlapped onto the velocity and vorticity contours, to better visualize the flow pattern. The velocity and vorticity contours for *We* = 60 and 80 are presented in this section.

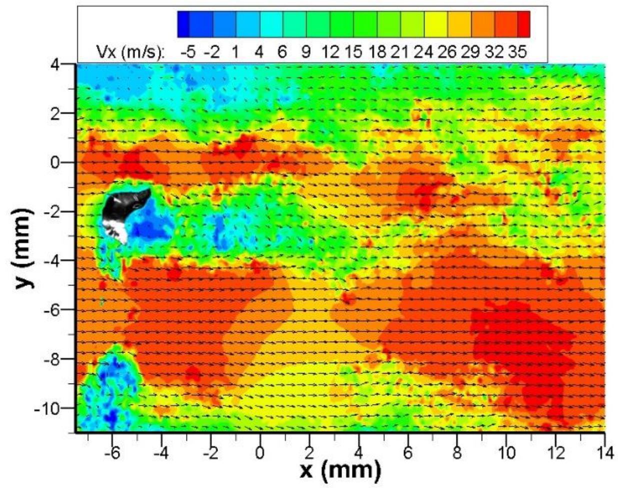

(a) t_1 = 3ms

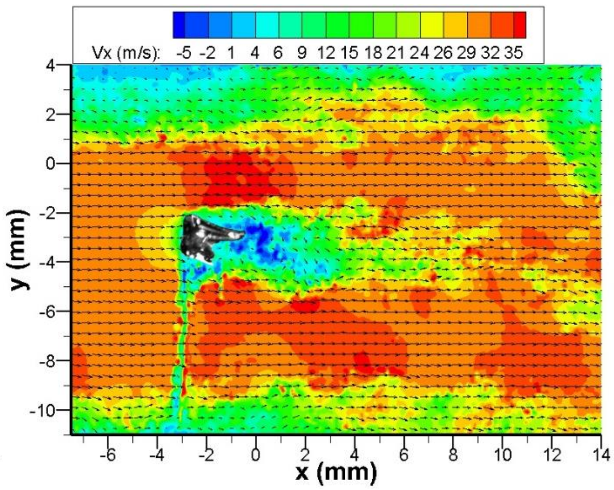

(b) t_2 = 4ms

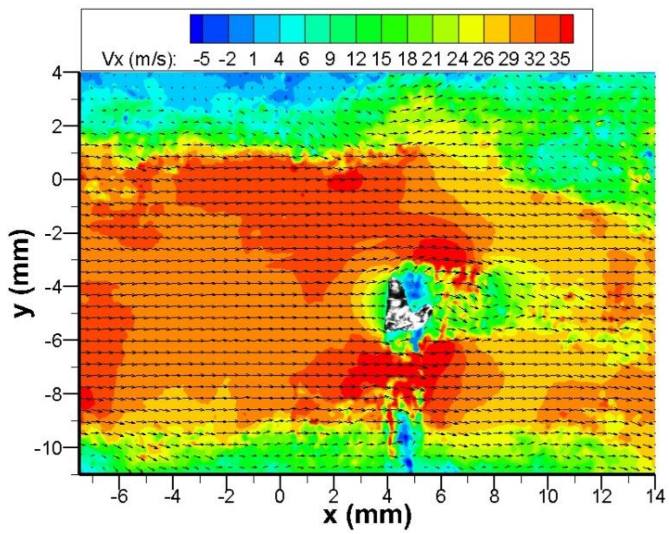

(c) t_3 = 5ms

Figure 4.28 Average velocity field of drop deformation at *We* = 60 at each instant of time.

Figure 4.28(a) is captured shortly after the droplet enters the air stream. Freestream velocity approximately 34 m/s can be observed for y < 1mm. X velocity decreases for y > 1mm due to the presence of a mixing layer. As time increases the droplet translates downstream. A strong wake region appears at t_1 and weakens with time. A backflow with V_x = -5 m/s appears at t_1. The backflow region spreads downstream at t_2 and diminishes at t_3 due to the geometry of the deformed droplet. However, the magnitude of the backflow remains the same with time. The backflow velocity corresponds to 15% of the free-stream velocity. The pressure difference between the stagnation region and wake zone isn't high enough for the droplet to form a bag. Hence, the droplet curls into itself to fill the relatively lower pressure pocket in the wake region. At t_3 the mixing layer is seen for $y < -8.5$mm. The viscosity of droplet also plays a major role in overcoming the aerodynamic forces. As the droplet curls into itself, a smaller area is exposed to the air stream and hence the dominant surface tension forces prohibit drop breakup. Additionally, vorticity contours for *We* = 60 (shown in figure 4.29) are evaluated to analyze the wake structure.

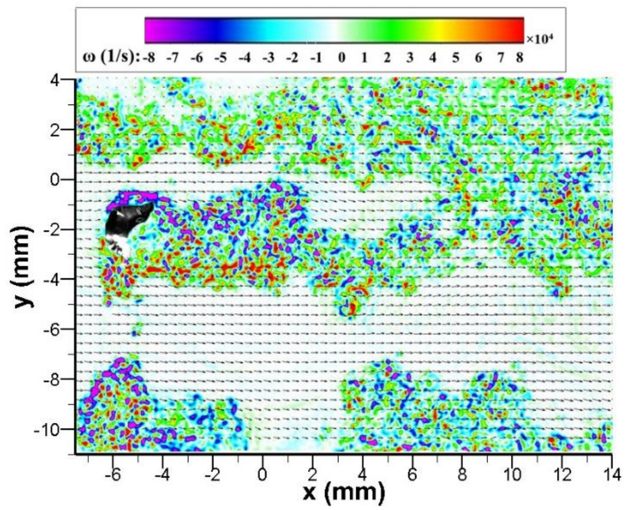

(a) t_1 = 3ms

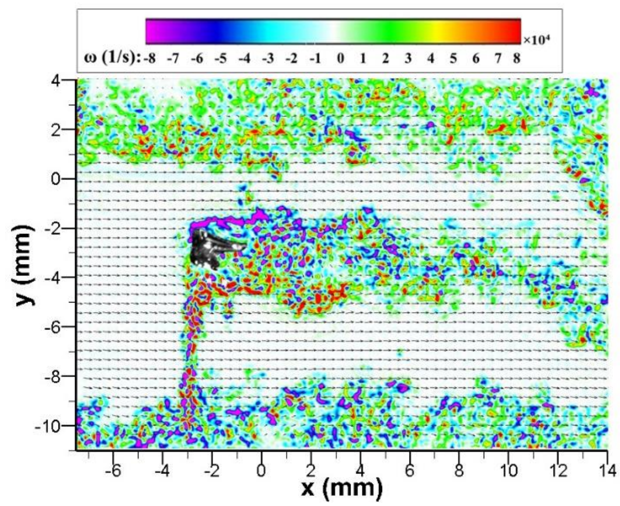

(b) t_2 = 4ms

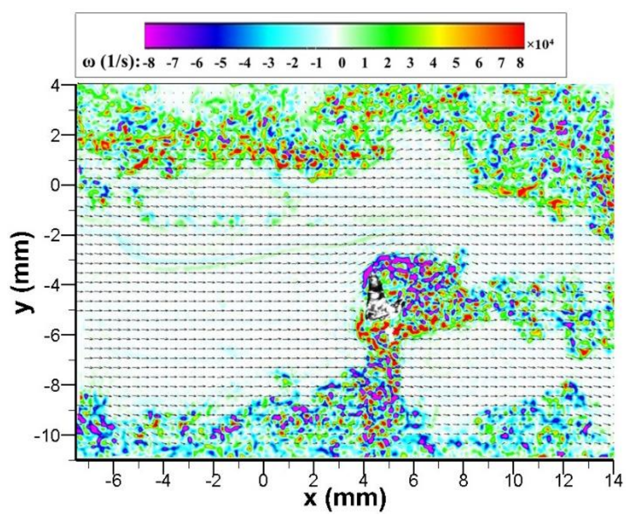

(c) t_3 = 5ms

Figure 4.29 Average vorticity field of drop deformation at *We* = 60 at each instant of time.

Vorticity pattern around a droplet is similar to the vortex structure formed around a sphere in a turbulent flow. Here, the flow itself is in 3D and the results presented are a 2D cross-sectional view of the flow. A similar vortex pattern is shown in figure 4.30 for a turbulent flow past a sphere.

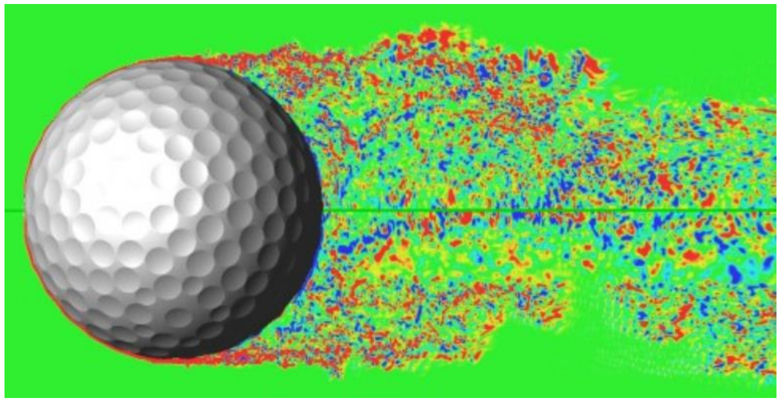

Figure 4.30 2D representation of vortices formed in a turbulent flow around a sphere. (seedgolf.com)

A few notable observations can be made from figure 4.29. Strong counteracting vortices can be seen on either ends of the droplet. This with an increase in time the vortex region diminishes. This could be due to the translation of the droplet downstream. Strong vortex shedding in the wake could be due to multiple reasons. The shape of the droplet, with sharp edges, could be a reason for the vortices to strip of at the rear end of the droplet. The high Reynolds number here makes the flow turbulent and mimics a vortex patter like that of a sphere. Hence, we do not observe a vortex pair like that of a laminar flow around a 2D cylinder. The counter acting vortices are continuous at the droplet periphery before the shed down into the turbulent wake. This strong counteracting force could be a reason for the edges to bend into itself. Vortices are seen in figure 4.28 (a) and (b) for $y > 1$ mm and $y < -8.5$mm respectively. This is again due to the mixing layer. The freestream zone is relatively vortex free. Vertical vortex line seen below the droplet is an inconsistency due to the shadow formed in the region of the laser sheet beneath the droplet.

For higher Weber number droplet exhibited multiple bag formation and breakup. PIV was done for $We = 80$ to draw a better comparison with $We = 60$ to better understand the reasons for a droplet to not breakup at $60 \leq We \leq 70$. PIV Results for $We = 80$ are presented below. Once again, velocity and vorticity contours are represented at different times. Bag breakup isn’t considered here due to the strong reflections from all the droplets. Hence, this study includes cases only until the time just before the bag rupture.

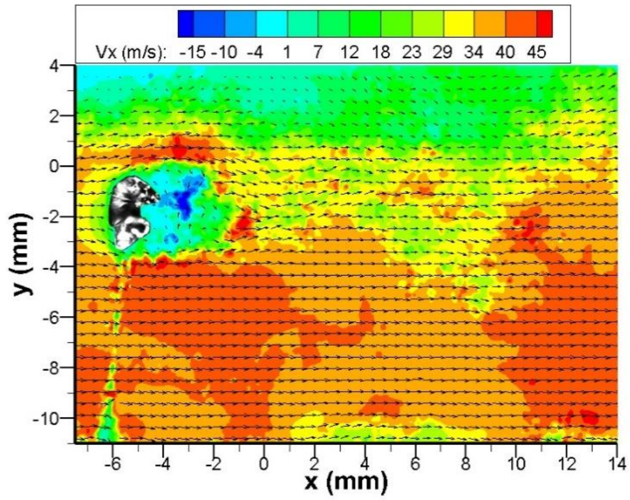

(a) t_1 = 3ms

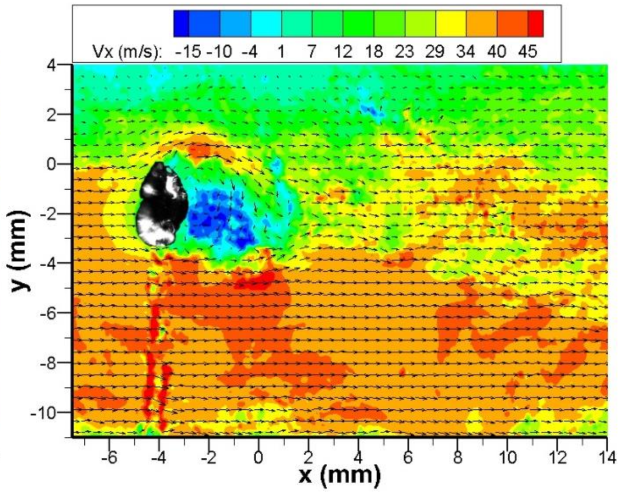

(b) t_2 = 3.5ms

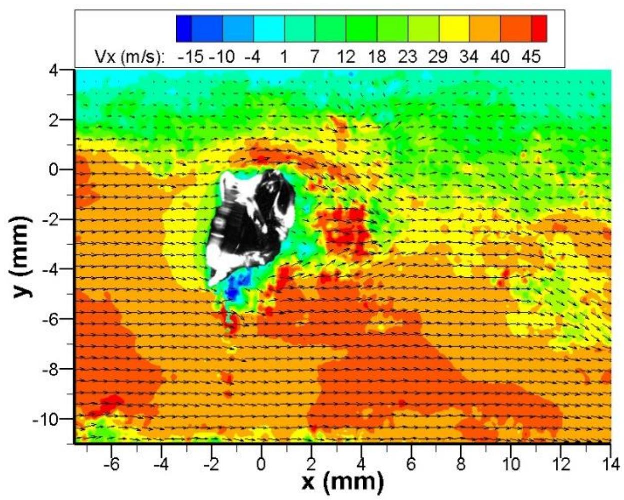

(c) t_3 = 4.5ms

Figure 4.31 Average velocity field of drop deformation at *We* = 80 at each instant of time.

For *We* = 80, at t_1 = 3ms the deformation is similar to that seen in figure 4.28(a). Low velocity can be seen in the mixing layer for y > 0. As time increases, the droplet translates downstream. However, the fall in negative y is minimal due to the dominance of V_x. The wake decreases over time as seen in the previous case. The backflow region increases from t_1 to t_2 and then vanishes at t_3. Again, the magnitude of the backflow remains same though it spreads into the wake. Here, the backflow velocity is measured to be approximately 15 m/s which accounts to 35% of the freestream velocity. As the droplet periphery rolls into itself, the stagnation pressure developed is high enough to form the bag. Therefore, bags are formed from both the droplet core and the curled in periphery leading to multiple bag breakup mode.

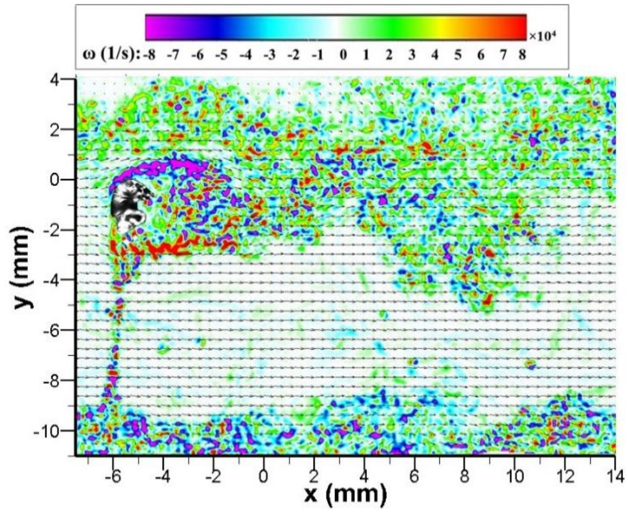

(a) t_1 = 3ms

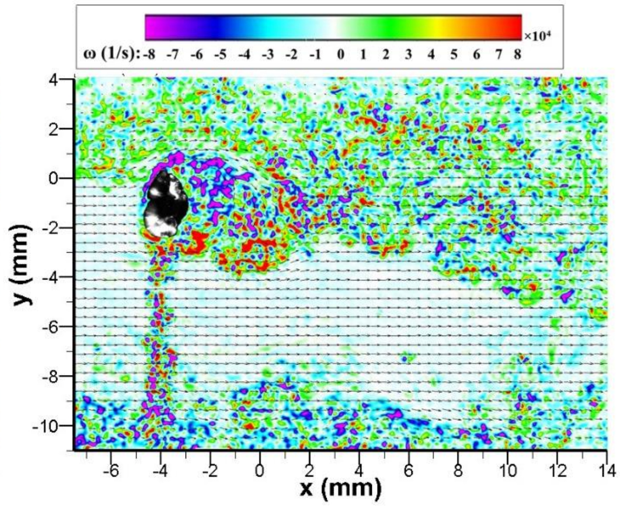

(b) t_2 = 3.5ms

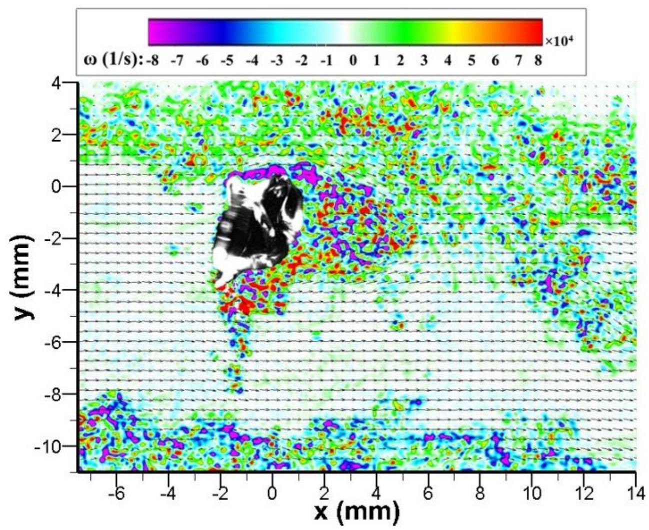

(c) t_3 = 4.5ms

Figure 4.32 Average vorticity field of drop deformation at *We* = 80 at each instant of time

Vorticity contours formed for *We* = 80 is similar to that seen in *We* = 60. Vortices can be seen for y > 0 in the mixing layer. Vortex region decreases with increase in time as droplet moves downstream. Strong counter acting vortices is again observed at drop periphery. Once again, the flow exhibits vortex shedding similar to that in a turbulent flow around a sphere.

The length of the vortex region is proportional to the wake zone. The development of the vortex region over time for varying weber number has been plotted in Figure 4.33. The vortex street length (λ_{vortex}) is normalized using the instantaneous drop cross-stream diameter d_{cro}.

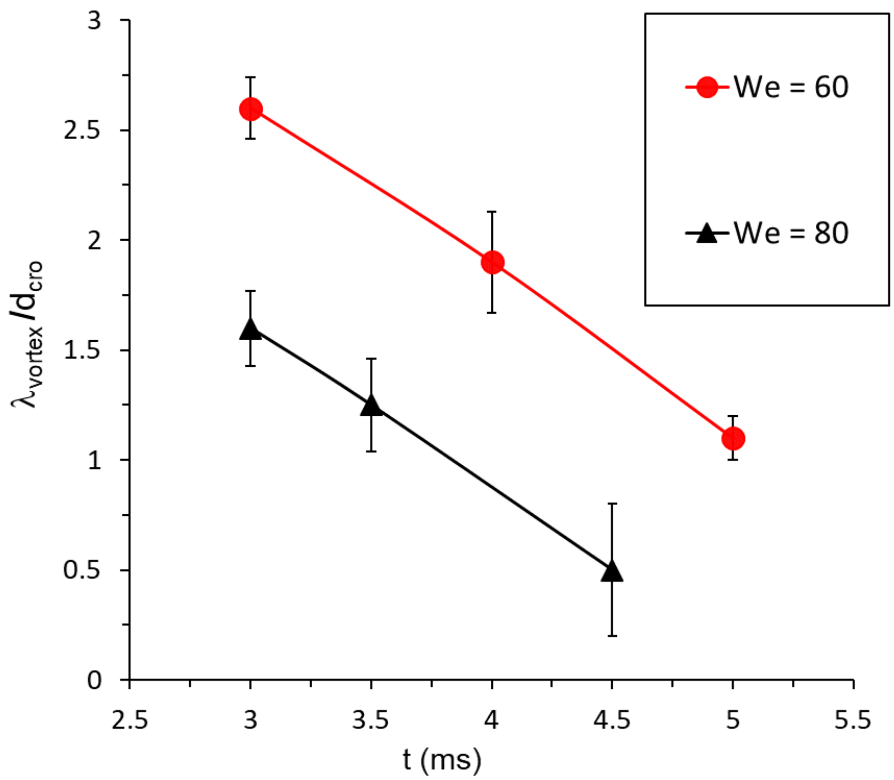

Figure 4.33 Vortex street length as a function of time for *We* = 60 and *We* = 80

λ_{vortex}/d_{cro} is evaluated for 200 PIV realizations at each time step. The average value and error bar have been plotted. It is seen that the length of the vortex zone decreases linearly with time. Hence the wake region decreases. These findings agree with the results presented above. Also, with an increase in Weber number the λ_{vortex}/d_{cro} decreases. As the Weber number increases, the turbulent Reynolds number increases, hence the wake zone decreases. This is also due to the increase in the instantaneous drop cross-stream diameter. The cross-stream diameter has a larger value at *We* = 80 compared to *We* = 60 due to the different droplet behaviors discussed in previous sections. The error at t_3 for *We* = 80 is relatively high due to the low repeatability of bag geometry. Since this is the time just before the droplet breakup, the uncertainty is relatively higher.

Figure 4.34 shows the percentage of backflow velocity at different Weber numbers. Results from Flock et al. (2012) have also been presented. It can be seen that droplet undergoes breakup only when the velocity of backflow, in the droplet wake, is at least 30% of the freestream velocity.

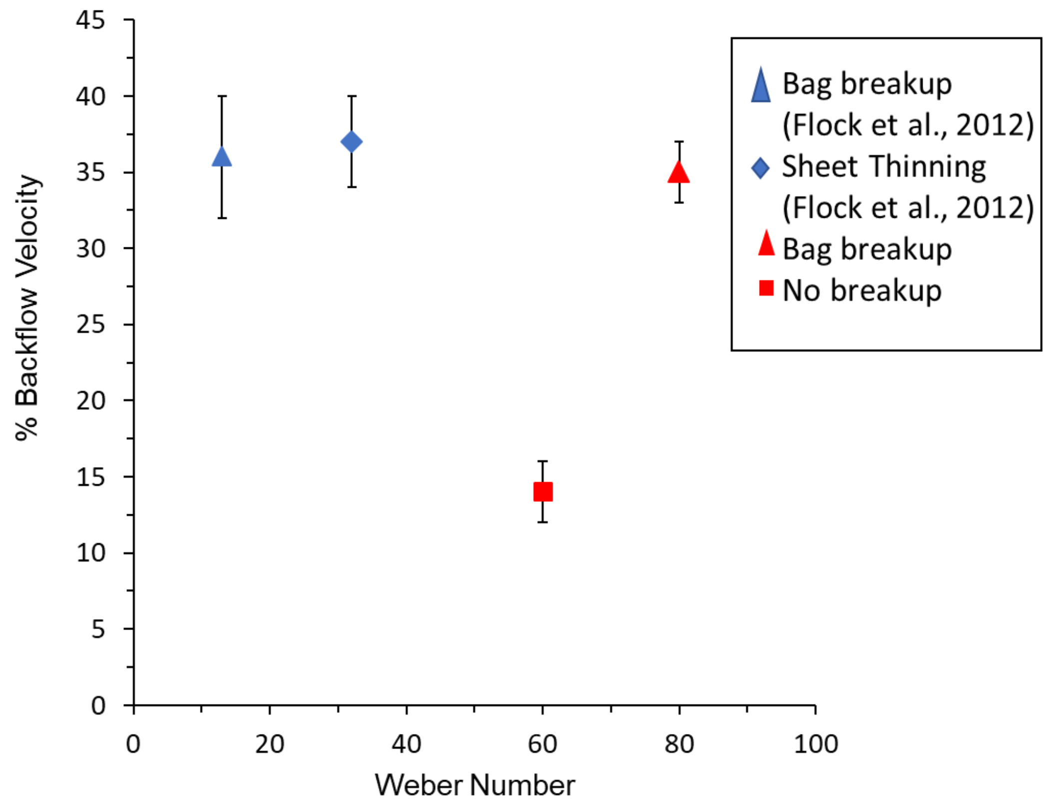

Figure 4.34 Percentage of Backflow for Various breakup modes

From the results above it can be asserted that one reason for the unique droplet behavior at $60 \leq We \leq 70$ could be due to the low pressure difference between the stagnation and wake region. Also, the backflow was only 14 % of the freestream velocity for *We* = 60 while it was 35 % for, *We* = 80. A.K. Flock *et al.* (2012), performed similar tests at low *Oh* and found that bag breakup mode exhibited at *We* = 13 had a similar backflow region with a velocity 30%-40% of the free stream velocity. Hence, it is reasonable to conclude that, bag formation requires a backflow with a magnitude of 30% to 40% of the freestream velocity to exist in the droplet wake to attain an appropriate pressure difference.

Additionally, it should be noted that there are a few factors that contribute to the uncertainty of the PIV results presented above. The multiphase flow problem at hand is complicated in itself to analyze using PIV. The liquid droplet reflects and refracts the laser sheet forming bright spots on the droplet obscuring the data near droplet. There is a shadow in the laser sheet formed below the droplet. Pre-processing of raw images can be done to enhance the image and reduce the uncertainties. Additionally, the uncertainty in droplet location can be a major hurdle in obtaining averaged results. Typical PIV noise sources such as background noise, peak-locking effects and displacement gradients (Raffel et al., 2007) are reduced but not eliminated by the use of advanced commercial cross-correlation algorithms.

To conclude, characterization of secondary atomization at high Ohnesorge numbers were done using three experimental techniques. Results of which, were presented in this chapter. Shadowgraphy was used to characterize the droplet behavior and the breakup modes exhibited with respect to the change in Weber number. Few cases where the droplet deformation and breakup deviated from the standard modes of drop breakup were reported. These findings serve as a novelty in the field of secondary atomization as very little research has been done at high Ohnesorge numbers. Additionally, digital in-line holography was carried out to characterize the size-velocity *pdfs*. Very limited data is available for droplet size and velocity distributions at high *Oh*. The results obtained using DIH were in good agreement with the derivations from shadowgraphy. Later on, particle image velocimetry was utilized to better explain the aerodynamic influence on drop deformation. This was done to study the air flow around droplet, especially in the case where no drop breakup occurs. PIV was used to compare this case with higher Weber number case where multiple bags were formed. Reasonable conclusions were drawn from each of the experimental technique. The following chapter presents a detailed overview of the summary and conclusions drawn from the current work.

CHAPTER 5. SUMMARY AND CONCLUSIONS

The preceding chapters discussed an experimental investigation into secondary atomization at high Ohnesorge numbers. The results are summarized in this chapter and recommendations are made for future work.

High-speed flow visualization was carried out to characterize droplet breakup at high ***Oh*** = 1. At Weber numbers 35 and 45, the breakup was similar to low ***Oh*** (<0.1) drops. However, at ***We*** > 50, the break up modes differed:

Drops further exhibited the multimode breakup where a bag and stamen were formed, the bag, however, underwent complete breakup, unlike the stamen. The stamen carried the droplet core and hence the number of fine droplets formed was lower compared to regimes at *We* > 80. A peculiar case, similar to vibrational mode at low ***Oh***, was found at Weber numbers past multimode breakup. The droplet periphery curved into itself, a smaller droplet area was exposed to the aerodynamic forces, and hence no breakup was observed. As We increased beyond a value of 80, peripheral bending (flapping) was observed, which is a deviation from breakup processes found in low ***Oh*** drops. This was due to the high viscosity of glycerine, which prohibited the formation of small drops from the drop equator. As ***We*** increased even further, the drops did not exhibit shear stripping which is observed at ***We*** = 80 for ***Oh*** < 0.1, as the aerodynamic forces were not sufficient to overcome the viscous forces at these values of ***Oh***. However, multiple bag formations took place. The bags were formed from both droplet core and periphery. Either the core broke up before bags formed from the periphery, or they all broke up at the same time. The latter occurred at ***We*** = 120, highest ***We*** considered. These observations have not been reported in the literature, and hence are novelties.

Further studies were carried out using DIH to analyze the size and velocity distributions of fragments formed from in the various regimes. Intermediate values of *Oh* were also considered.

DIH was carried out for a range of ***We*** at ***Oh*** = 0.5 and ***Oh*** = 1. It was found that liquid viscosity played a significant role in drop size distribution.

At $\boldsymbol{Oh}$ = 1 and 35 ≤ $\boldsymbol{We}$ ≤ 45, a bimodal distribution was displayed signifying the formation of large fragments from the toroidal ring and stamen in the bag and multimode regimes, respectively. With increasing $\boldsymbol{We}$, a mono-modal distribution was seen. Large numbers of droplets were formed from the multiple bag breakup at Weber numbers greater than 80: at $\boldsymbol{We}$ = 80 the size distribution peaked between drop diameters of 110 and 160 μm. As $\boldsymbol{We}$ increased to 120, the size of the droplets formed reduced to 110 μm due to the dominance of aerodynamic forces.

At $\boldsymbol{Oh}$ = 0.5, peak distributions similar to $\boldsymbol{Oh}$ = 1 were noted. However, the considerable amount of large size droplets at $\boldsymbol{We}$ ≥ 80 for $\boldsymbol{Oh}$ = 0.5 This is since, at $\boldsymbol{Oh}$ = 0.5, a thicker rim and a smaller bag is formed, where the rim contributes to larger drops and the latter contributes to fine secondary drops. In contrast, at $\boldsymbol{Oh}$ = 1, the higher viscosity of the fluid favours larger bag formation, and the rim formed is relatively thin. Hence, we observe only very few large sized drops from the rim and maximum small sized drops from the bag.

From the velocity distributions presented, it can be concluded that as $\boldsymbol{We}$ increases a majority of the secondary drops attain a stable velocity. At $\boldsymbol{We}$ = 35 and 45, as the bag dissociates, the aerodynamic forces aren't high enough to produce very fine droplets. Hence a wider distribution is noted. With an increase in time, the larger fragments dissociate and the distribution narrows to a stable peak.

As $\boldsymbol{We}$ increases above 80, it can be seen that the droplets accelerate during disintegration and then decelerate once they have attained their peak velocity. Additionally, the distribution widens as time increases since the toroidal rim breaks up to produce fragments of larger sizes while bag disintegration leads to a narrower droplet size distribution. Additionally, at maximum tested $\boldsymbol{We}$ of 120, the velocity distribution remains uniform as the disruptive forces are high enough to completely disintegrate the bag and the rim to small fragments.

At $\boldsymbol{Oh}$ = 0.5, similar velocity distribution trends can be observed. However, at a particular time, wider distribution can be seen compared to $\boldsymbol{Oh}$ = 1. This mainly because, the droplet disintegrates sooner due to the lower viscosity at Oh = 0.5, producing more droplets with varying velocity at a given time. Therefore, at a particular time step, a drop at $\boldsymbol{Oh}$ = 0.5 will undergo more breakup than a drop at $\boldsymbol{Oh}$ = 1.

PIV results provide a fundamental understanding regarding the flow behaviour. It can be concluded that bag formation requires a back flow in the wake region, with a velocity at least 30% of the freestream velocity. In addition, 2D representation of 3D vortex structures were displayed, which was never done in the past. A linear relationship was established between the length of the vortex zone and time for varying $\boldsymbol{We}$.

5.1 Future Work

As a plenty of work isn't available on secondary atomization at high Ohnesorge number, this work served as a beginning point for researchers to further work in this field and validate their results. A few recommendations for future work are given below to further explore this field of research.

The current work was limited to We = 120. In future, similar tests could be carried out for higher weber numbers to characterize the sheet thinning and catastrophic mode breakup at high Ohnesorge numbers. Droplet size-velocity distributions at higher weber numbers would help industries utilize the data for applications where the relative velocities are really high. Characterization of breakup at higher Weber numbers would enable to complete a chart representing the transition Weber numbers for viscous fluids. This will enable to present a strong reliable data to characterize secondary breakup at high Oh.

Further, testing liquids with higher viscosity would serve as a good experiment to fill the existing void in the literature. Higher Oh drops require higher air velocities to undergo breakup. Current setup is limited by the Weber number range and hence liquids with Oh greater than 2 could not be tested as no breakup was seen until We = 120. Additionally, drop parameters such as surface tension and drop size can be varied to better characterize the influence of viscosity at a given Oh.

Current PIV setup utilizes only one laser sheet to visualize the air flow around the droplet. A setup with twin laser sheets could be utilized to avoid the uncertainties due to the droplet shadow in the PIV data. Additionally, a 3D analysis of the flow could be carried out using the state of the art PIV commercial setups in order to characterize the velocity and pressure distribution around the droplet.

LIST OF REFERENCES

Aalburg, C., van Leer, B. and Faeth, G. M., 2003, "Deformation and Drag Properties of Round Drops Subjected to Shock-Wave Disturbances," *AIAA Journal*, vol. 41(12), pp. 2371-2378.

Babinsky, E. and Sojka, P. E., 2002, "Modeling Drop Size Distributions," *Progress in Energy and Combustion Science*, vol. 28, pp. 303-329.

Cousin, J., Yoon, S. J. and Dumouchel, C., 1996, "Coupling of Classical Linear Theory and Maximum Entropy Formalism for Prediction of Drop Size Distribution in Sprays: Application to Pressure-Swirl Atomizers," *Atomization and Sprays*, vol. 6, pp. 601-622.

Déchelette, A., Babinsky, E. and Sojka, P.E., 2011. Drop size distributions. In *Handbook of Atomization and Sprays* (pp. 479-495). Springer, Boston, MA.

Dumouchel, C., 2006, "A New Formulation of the Maximum Entropy Formalism to Model Liquid Spray Drop-Size Distribution," *Particle and Particle Systems Characterization*, vol. 23, pp. 468-479.

Dumouchel, C. and Boyaval, S., 1999, "Use of the Maximum Entropy Formalism to Determine Drop Size Characteristics," *Particle and Particle Systems Characterization*, vol. 16, pp. 177-184.

Faeth, G. M., Hsiang, L. P. and Wu, P. K., 1995, "Structure and Breakup Properties of Sprays," *International Journal of Multiphase Flow*, vol. 21(Suppl. S), pp. 99-127.

Flock, A.K., Guildenbecher, D.R., Chen, J., Sojka, P.E. and Bauer, H.J., 2012. "Experimental statistics of droplet trajectory and air flow during aerodynamic fragmentation of liquid drops," *International journal of multiphase flow*, *47*, pp.37-49.

Gao, J., Guildenbecher, D.R., Reu, P.L., Kulkarni, V., Sojka, P.E. and Chen, J., 2013. "Quantitative, three-dimensional diagnostics of multiphase drop fragmentation via digital in-line holography," *Optics letters*, *38*(11), pp.1893-1895.

Gelfand, B. E., 1996, "Droplet Breakup Phenomena in Flows with Velocity Lag," *Progress in Energy Combustion Science*, vol. 22, pp. 201-265.

Guildenbecher, D.R., López-Rivera, C. and Sojka, P.E., 2009, "Secondary atomization. *Experiments in Fluids*," *46*(3), p.371.

Guildenbecher, D.R., 2009, "Secondary atomization of electrostatically charged drops," Thesis.

Guildenbecher, D.R. and Sojka, P.E., 2011, "Experimental investigation of aerodynamic fragmentation of liquid drops modified by electrostatic surface charge," *Atomization and Sprays*, *21*(2).

Guildenbecher, D.R., Gao, J., Reu, P.L. and Chen, J., 2012, September, “Digital holography reconstruction algorithms to estimate the morphology and depth of nonspherical absorbing particles,” In *Interferometry XVI: Techniques and Analysis* (Vol. 8493, p. 849303). International Society for Optics and Photonics.

Guildenbecher, D.R., Engvall, L., Gao, J., Grasser, T.W., Reu, P.L. and Chen, J., 2014, “Digital in-line holography to quantify secondary droplets from the impact of a single drop on a thin film,” *Experiments in fluids*, *55*(3), p.1670.

Guildenbecher, D.R. and Sojka, P.E., 2015. *Demonstration of High Speed (20 kHz) Digital Inline Holographic (DIH) Imaging of a Multiphase Event*: Drop Impact on a Thin Liquid Film (No. SAND2015-2423C). Sandia National Lab.(SNL-NM), Albuquerque, NM (United States).

Han, J. and Tryggvason, G., 2001, “Secondary Breakup of Axisymmetric Liquid Drops. II. Impulsive Acceleration,” *Physics of Fluids*, vol. 13(6), pp. 1554-1565.

Hsiang, L. P. and Faeth, G. M., 1992, “Near-Limit Drop Deformation and Secondary Breakup,” *International Journal of Multiphase Flow*, vol. 18(5), pp. 635-652.

Hsiang, L. P. and Faeth, G. M., 1993, “Drop Properties after Secondary Breakup,” *International Journal of Multiphase Flow*, vol. 19(5), pp. 721-735.

Hsiang, L. P. and Faeth, G. M., 1995, “Drop Deformation and Breakup Due to Shock Wave and Steady Disturbances,” *International Journal of Multiphase Flow*, vol. 21(4), pp. 545-560.

Inamura, T., Yanaoka, H. and Kawada, T., 2009, “Visualization of airflow around a single droplet deformed in an airstream,” *Atomization and Sprays*, *19*(7).

Jiang, L. and Agrawal, A.K., 2015, “Investigation of glycerol atomization in the near-field of a flow-blurring injector using time-resolved piv and high-speed visualization,” *Flow, Turbulence and Combustion*, *94*(2), pp.323-338.

Joseph, D. D., Belanger, J. and Beavers, G. S., 1999, “Breakup of a Liquid Drop Suddenly Exposed to a High-Speed Airstream,” *International Journal of Multiphase Flow*, vol. 25, pp. 1263-1303.

Krzeczkowski, S. A., 1980, “Measurement of Liquid Droplet Disintegration Mechanisms,” *International Journal of Multiphase Flow*, vol. 6, pp. 227-239.

Liu, A. B. and Reitz, R. D., 1993, “Mechanisms of Air-Assisted Liquid Atomization,” *Atomization and Sprays*, vol. 3, pp. 55-75.

Lopez Rivera, C., 2010, “*Secondary breakup of inelastic non-Newtonian liquid drops*,” Thesis.

Pilch, M. and Erdman, C. A., 1987, "Use of Breakup Time Data and Velocity History Data to Predict the Maximum Size of Stable Fragments for Acceleration-Induced Breakup of a Liquid Drop," *International Journal of Multiphase Flow*, vol. 13(6), pp. 741-757.

Ranger, A. A. and Nicholls, J. A., 1969, "Aerodynamic Shattering of Liquid Drops," *AIAA Journal*, vol. 7(2), pp. 285-290.

Simmons, H. C., 1977a, "The Correlation of Drop-Size Distributions in Fuel Nozzle Sprays. Part I: The Drop-Size/Volume-Fraction Distribution," *Journal of Engineering for Power-Transactions of the ASME*, vol. 99(3), pp. 309-314.

Simmons, H. C., 1977b, "The Correlation of Drop-Size Distributions in Fuel Nozzle Sprays. Part II: The Drop-Size/Number Distribution," *Journal of Engineering for PowerTransactions of the ASME*, vol. 99(3), pp. 315-319.

Tate, R.W. and Marshall, W.R., 1953, "Atomization by Centrifugal Pressure Nozzles. 2," *Chemical Engineering Progress*, *49*(5), pp.226-234.

Theofanous, T. G., Li, G. J. and Dinh, T. N., 2004, "Aerobreakup in Rarefied Supersonic Gas Flows," *Journal of Fluids Engineering-Transactions of the ASME*, vol. 126(4), pp. 516-527.

Zhou, W., Zhao, T., Wu, T. and Yu, Z., 2000, "Application of Fractal Geometry to Atomization Process," *Chemical Engineering Journal*, vol. 78(2-3), pp. 193-197.